

**A-15 type superconducting hydride La<sub>4</sub>H<sub>23</sub>: Nanograined structure with low strain, strong electron-phonon interaction, and moderate level of nonadiabaticity**

Evgeny F. Talantsev<sup>1,2</sup> and Vasilij V. Chistyakov<sup>1,2</sup>

<sup>1</sup>M.N. Miheev Institute of Metal Physics, Ural Branch, Russian Academy of Sciences, 18, S. Kovalevskoy St., Ekaterinburg, 620108, Russia

<sup>2</sup>NANOTECH Centre, Ural Federal University, 19 Mira St., Ekaterinburg, 620002, Russia

**Abstract**

For seven decades by A-15 superconductors we meant metallic A<sub>3</sub>B alloys (where A is a transition metal, and B is groups IIIB and IVB element) discovered by Hardy and Hulm (*Phys. Rev.* **89**, 884 (1953)). Nb<sub>3</sub>Ge exhibited the highest superconducting transition temperature,  $T_c = 23$  K, among these alloys. One of these alloys, Nb<sub>3</sub>Sn, is primary material in modern applied superconductivity. Recently Guo *et al* (*arXiv:2307.13067*) extended the family of superconductors where the metallic ions arranged in the beta tungsten (A-15) sublattice by observation of  $T_{c,zero} = 81$  K in La<sub>4</sub>H<sub>23</sub> phase compressed at  $P = 118$  GPa. Despite the La<sub>4</sub>H<sub>23</sub> has much lower  $T_c$  in comparison with near-room-temperature superconducting LaH<sub>10</sub> phase ( $T_{c,zero} = 250$  K at  $P \sim 200$  GPa) discovered by Drozdov *et al* (*Nature* **569**, 531 (2019)), the La<sub>4</sub>H<sub>23</sub> holds the record high  $T_c$  within A-15 family. Cross *et al* (*Phys. Rev. B* **109**, L020503 (2024)) confirmed the high-temperature superconductivity in the compressed La<sub>4</sub>H<sub>23</sub>. In this paper, we analyzed available experimental data measured in La<sub>4</sub>H<sub>23</sub> and found that this superconductor exhibits nanograined structure,  $6 \text{ nm} \leq D \leq 27 \text{ nm}$ , low crystalline strain,  $|\varepsilon| \leq 0.005$ , high electron-phonon coupling constant,  $2.1 \leq \lambda_{e-ph}(98 \text{ GPa}) \leq 2.7$ , and moderate level of the nonadiabaticity,  $0.18 \leq \Theta_D/T_F \leq 0.24$  (where  $\Theta_D$  is the Debye temperature, and  $T_F$  is the Fermi temperature). We found that derived  $\Theta_D/T_F$  and  $T_c/T_F$  values for the La<sub>4</sub>H<sub>23</sub> phase are similar to the ones in cuprates, pnictides, and near-room-temperature superconductors H<sub>3</sub>S and LaH<sub>10</sub>, which implies that the La<sub>4</sub>H<sub>23</sub> phase falls to unconventional superconductors band in the Uemura plot.

## **A-15 type superconducting hydride La<sub>4</sub>H<sub>23</sub>: Nanograined structure with low strain, strong electron-phonon interaction, and moderate level of nonadiabaticity**

### **I. Introduction**

In 1953 Hardy and Hulm<sup>1</sup> discovered that A<sub>3</sub>B alloys (where A is one of the transition metals Ti, Zr, V, Nb, Ta, Cr, and Mo, and B is one element of groups IIIB and IVB, or the precious metals Os, Ir, Pt, and Au<sup>2</sup>) with A-15 lattice exhibit the superconducting transition temperature up to  $T_c = 23$  K (for Nb<sub>3</sub>Ge<sup>3</sup>) and high values for low-temperature upper critical field,  $B_{c2}(4.2\text{ K}) \sim 37$  T (for Nb<sub>3</sub>Ge<sup>4</sup>). One of these alloys, Nb<sub>3</sub>Sn, is primary material for superconducting wires in nearly all modern commercial magnetic systems, including magnetic systems for mega-science projects<sup>5-37</sup>.

Near-room temperature superconductivity in superhydrides was experimentally discovered by Drozdov *et al*<sup>38</sup>, and LaH<sub>10</sub> holds record high  $T_c$  (with  $T_{c,onset} = 280$  K<sup>39,40</sup> at pressure  $P \sim 200$  GPa) for ever known superconductors. The La-H binary system has a very rich phase diagram<sup>39-42</sup>, and this was already showed in the first study by Drozdov *et al*<sup>38</sup>. In the extended study by Sakata *et al*<sup>41</sup> this feature of the La-H system has been shown with great clarity by reporting at least five fundamentally different XRD scans (which means that samples contain different LaH<sub>x</sub> phases) for samples with the onset transition temperatures within a range of  $65\text{ K} \leq T_{c,onset} \leq 112\text{ K}$ . Later the crystalline structure for seven high-pressure La<sub>x</sub>H<sub>y</sub> phases have been identified by Laniel *et al*<sup>42</sup>,

Recently Guo *et al*<sup>43</sup> showed that there is a superhydride phase in La-H binary system, with stoichiometry of La<sub>4</sub>H<sub>23</sub>, exhibits A-15 (beta tungsten) arrangement of lanthanum ions. This phase exhibits  $T_{c,zero} = 81$  K at pressure  $P = 118$  GPa. Thus, the A-15 superconductor family can be extended by the La<sub>4</sub>H<sub>23</sub> phase. Despite the La<sub>4</sub>H<sub>23</sub> has much lower  $T_c$  in comparison with its near-room-temperature counterpart LaH<sub>10</sub>, the La<sub>4</sub>H<sub>23</sub> holds the record high  $T_c$  within A-15 family.

Soon, after the report by Guo *et al*<sup>43</sup>, Cross *et al*<sup>44</sup> confirmed the high-temperature superconductivity in highly compressed La<sub>4</sub>H<sub>23</sub> phase with measured  $T_{c,R \rightarrow 0 \Omega} \cong 60 \text{ K}$  ( $P = 95 \text{ GPa}$ ), which was defined by strict resistive criterion:

$$\frac{|R(T) - R(T_{c,onset})|}{R(T_{c,onset})} \leq 1 \times 10^{-3} \quad (1)$$

Recently two research groups<sup>45,46</sup> specialized in the first-principles calculations of high-pressure superconductors showed that the transition temperature of highly compressed superconductors should be impacted by the crystalline lattice distortions (caused by either the presence of vacancies<sup>45</sup>, either by the anisotropic crystalline strain<sup>46</sup>). Considering that there is a dependence of the Debye temperature,  $\Theta_D$ , from the size of the crystals<sup>47</sup>, in this study we continue<sup>48</sup> to extract the size and the strain in highly pressurized superconductors from the XRD data, because these parameters can be characteristics which can enrich our understanding of the near-room-temperature superconductivity.

Thus, in this paper, we analyzed available experimental data measured in La<sub>4</sub>H<sub>23</sub> by two research groups<sup>43,44</sup>, and we found that this superconducting phase exhibits:

1. Nanograined structure, with average size of coherent-scattering regions,  $D$ , varied in the range  $6 \text{ nm} \leq D \leq 27 \text{ nm}$ ;
2. Low nanocrystalline strain,  $\varepsilon$ , which is varied in the range  $-0.003 \leq \varepsilon \leq 0.005$  (where negative  $\varepsilon$  can be interpreted as the state with high concentrations of hydrogen vacancies);
3. Relatively low Debye temperatures,  $\Theta_D(P = 95 \text{ GPa}) \cong 500 \text{ K}$ , and  $\Theta_D(P = 118 \text{ GPa}) \cong 900 \text{ K}$ , which implies that the La<sub>4</sub>H<sub>23</sub> is strong coupled superconductor with high electron-phonon coupling constant  $1.5 \leq \lambda_{e-ph} \leq 2.7$ ;
4. Moderate level of the nonadiabaticity,  $0.22 \leq \frac{\Theta_D}{T_F} \leq 0.24$  (where  $T_F$  is the Fermi temperature).

5. Deduced ratio of  $0.02 \leq \frac{T_c}{T_F} \leq 0.03$  implies that the La<sub>4</sub>H<sub>23</sub> phase falls to unconventional superconductors band in the Uemura plot.

## II. Experimental data sources and data analysis tool

Primarily, we performed an analysis for experimental datasets provided by Cross *et al*<sup>44</sup> as free online experimental data source at the University of Bristol data center<sup>44</sup>. Data for Guo *et al*<sup>43</sup> report was digitized from original plots in the paper<sup>43</sup>. Used models and mathematical routines for the analysis described within each section. All fits performed in the Origin software.

## III. Results

### 3.1. La<sub>4</sub>H<sub>23</sub> ( $P = 95$ GPa)

#### 3.1.1. Size-strain analysis

There are no direct macroscopical techniques which can be applied to study the microstructure (at the submicron level) of the sample in the diamond anvil cell (DAC). However, primary structural parameters of the sample can be extracted from classical Williamson-Hall (WH) analysis<sup>49</sup> of the X-ray diffraction (XRD) data.

We fitted XRD scans to multiple peaks Lorentz function (Figure S1):

$$I(2\theta) = I_{background} + \sum_{i=1}^N \frac{2 \times A_i}{\pi} \times \frac{\beta_i}{4 \times (2\theta - 2\theta_{peak,i})^2 + \beta_i^2}, \quad (2)$$

where  $A_i$ ,  $2\theta_{peak,i}$ ,  $\beta_i$ , are-free fitting parameters, and we manually adjusted the  $I_{background}$  level for each panel showed in all figures in this study.

In Figure 1 we showed the fit of the XRD data reported by Cross *et al*<sup>44</sup> to Eq. 2, where we designated by thick red curves all peaks described by Cross *et al*<sup>44</sup> as peaks for the La<sub>4</sub>H<sub>23</sub> phase. One can see (Figure 1) that there are many peaks which were not designated to the La<sub>4</sub>H<sub>23</sub> phase by Cross *et al*<sup>44</sup>. This is another confirmation of the findings by Laniel *et al*<sup>42</sup>,

that there are several La-H phases which can exist simultaneously in the DAC sample.

However, we should stress that as it showed by first principles calculations by Guo *et al*<sup>43</sup>, high-temperature superconductivity is associated exclusively with the La<sub>4</sub>H<sub>23</sub> phase at the pressure range of around 100 GPa.

Derived dataset for the peak breadth,  $\beta_i(\theta)$ , and peak diffraction angle,  $\theta_{peak,i}$ , for the La<sub>4</sub>H<sub>23</sub> phase was fitted to WH equation<sup>49</sup> (where we assumed that the instrumental broadening,  $\beta_{instrumental}$ , is negligible):

$$\beta(\theta, P) = \frac{0.9 \times \lambda_{x-ray}}{D(P) \times \cos(\theta)} + 4 \times \varepsilon(P) \times \tan(\theta), \quad (3)$$

where  $\lambda_{x-ray} = 42.5 \text{ pm}$  is the wavelength of the radiation used in Ref.<sup>44</sup>, and  $D(P)$  is the mean size of coherent scattering regions, and the  $\varepsilon(P)$  is the nanocrystalline strain.

Three fits of the  $\beta(\theta, P = 95 \text{ GPa})$  data to Eq. 3 are shown in Figure 1.

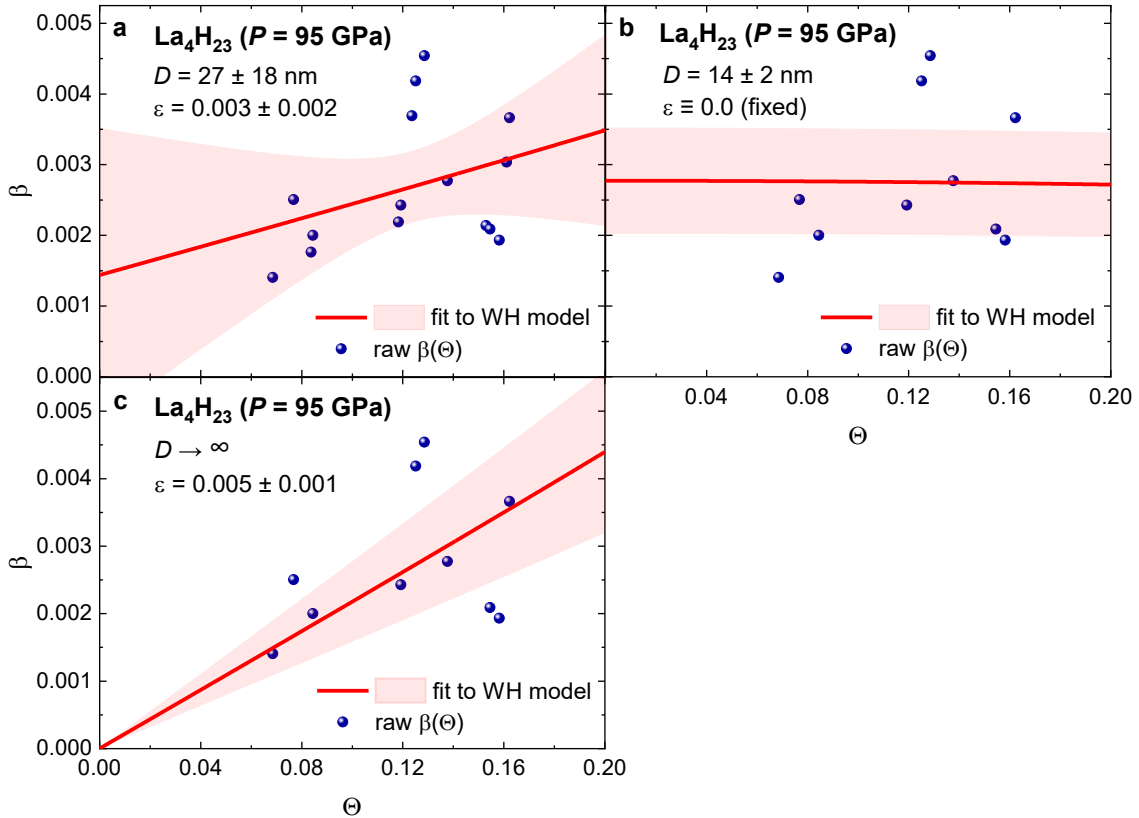


**Figure 1.** XRD peaks breadth,  $\beta(\theta)$ , and data fits to the Williamson-Hall equation (Eq. 3) for highly compressed single crystal La<sub>4</sub>H<sub>23</sub>. Raw XRD scans reported by Cross *et al*<sup>44</sup>. 95% confidence bands are shown by pink areas. (a)  $\beta(\theta, P)$  data fit to Eq. 3 when  $D(P)$  and  $\varepsilon(P)$  are free-fitting parameters. (b)  $\beta(\theta, P)$  data fit to Eq. 3 for the condition  $\varepsilon(P) \equiv 0$ . (c)  $\beta(\theta, P)$  data fit to Eq. 3 for the condition  $D(P) \rightarrow \infty$ .

In Figure 1a we showed the fit for which both  $D(P = 95 \text{ GPa})$  and  $\varepsilon(P = 95 \text{ GPa})$  are free-fitting parameters where one can see that  $2\sigma$  uncertainties for both values are large. Based on that in Figure 1b we restricted the fit to reveal the minimum size of the nanocrystals  $D_{min}(P = 95 \text{ GPa}) = 14 \pm 2 \text{ nm}$  (by applying the condition of  $\varepsilon(P = 95 \text{ GPa}) \equiv 0$ ). In Figure 1c we restricted the fit to reveal the maximum of the strain in nanocrystals,  $\varepsilon_{max}(P = 95 \text{ GPa}) = 0.005 \pm 0.001$  (by applying the condition of  $D(P = 95 \text{ GPa}) \rightarrow \infty$ ).

In overall (Figure 1), our analysis showed that the nanocrystalline strain in the  $\text{La}_4\text{H}_{23}$  phase at  $P = 95 \text{ GPa}$  is low, because its maximum possible value of  $\varepsilon_{max}(P = 95 \text{ GPa}) = 0.005 \pm 0.001$  is approximately equal to the value determine by the same WH technique in high-quality epitaxial undoped  $\text{YBa}_2\text{Cu}_3\text{O}_{7-\delta}$  films<sup>50</sup>.

We found that the  $\text{La}_4\text{H}_{23}$  phase is nanograined, and we found that the minimal grains size is  $D_{min} = (23 \pm 3) \times a$ , where  $a = 6.191(4) \text{ \AA}$  is the unit cell parameter<sup>44</sup>, and the grain size (when both parameters in the WH equation are free) is  $D = (43 \pm 29) \times a$ .

### 3.1.2. Debye temperature

*De facto* the standard technique to determine the Debye temperature,  $\Theta_D$ , for samples in DAC<sup>51-53</sup> is the fit of the temperature dependent resistance,  $R(T)$ , to the saturated resistance model<sup>54-56</sup> (where the  $\Theta_D$  is a free-fitting parameter):

$$R(T) = \frac{1}{\frac{1}{R_{sat}} + \frac{1}{\left( R_n + A \times \left( \frac{T}{\Theta_D} \right)^5 \times \int_0^{\frac{\Theta_D}{T}} \frac{x^5}{(e^x - 1)(1 - e^{-x})} dx \right)}} \quad (4)$$

where  $R_{sat}$ ,  $R_n$ ,  $A$ , and  $T_c$  are free-fitting parameters.

Recently Watanabe *et al*<sup>57</sup> reported a very good agreement between the  $\Theta_D$  deduced from the fit of the  $R(T)$  data to the reduced form of the Eq. 4 (for  $T \geq T_c$ , which implies that the only normal part of the  $R(T)$  curve was fitted) and by the fit of the total specific heat

capacity,  $C_p(T)$ , in the  $\eta$ -carbide-type oxide  $Zr_4Pd_2O$ . We can mention that the latter technique, the  $C_p(T)$  is fitted to the equation:

$$C_p(T) = \gamma \times T + \beta \times T^3 + \delta \times T^5 \quad (5)$$

where  $\gamma$  is the Sommerfeld coefficient,  $\beta$  and  $\delta$  are the amplitudes of the phonon contributions for the harmonic and anharmonic terms, respectively; and where the  $\Theta_D$  is calculated by applying equation:

$$\Theta_D = \left( \frac{12\pi^4 N R_{gc}}{5\beta} \right)^{\frac{1}{3}} \quad (6)$$

where  $N$  is the number of atoms per formula unit and  $R_{gc} = 8.31 \text{ JK}^{-1}\text{mol}^{-1}$  is the universal gas constant. It should be noted that the approach expressed by Eqs. 5-6 is the standard way to determine the Debye temperature from the total specific heat data<sup>57-64</sup>.

Advanced approach<sup>65-67</sup> is to fit the  $C_p(T)$  data to multichannel Debye-Einstein equation:

$$C_p(T) = \gamma \times T + 9 \times R_{gc} \times \sum_{i=1}^N A_i \left( \frac{T}{\Theta_{D,i}} \right)^3 \int_0^{\frac{\Theta_{D,i}}{T}} \frac{x^4 e^x}{(e^x - 1)^2} dx + 3 \times R_{gc} \times \sum_{j=1}^M B_j \left( \frac{\Theta_{E,j}}{T} \right)^2 \frac{e^{\left(\frac{\Theta_{E,j}}{T}\right)}}{\left( e^{\left(\frac{\Theta_{E,j}}{T}\right)} - 1 \right)^2} \quad (7)$$

where  $A_i$  and  $B_j$  are constants (depended from given crystalline structure and chemical composition),  $N$  and  $M$  are number of the channels for the Debye modes and the Einstein modes, respectively;  $\Theta_{D,i}$  is the Debye temperature of the  $i$ -channel,  $\Theta_{E,j}$  is the Einstein temperature of the  $j$ -channel. The use of the Eq. 7 requires high sensitivity measurements of the  $C_p(T)$  and an addition, all measurements should be performed in a wide temperature range,  $0 < T \lesssim \Theta_E$ , with a small temperature step,  $\Delta T \sim \frac{\Theta_D}{500}$ , between measurements, at least in low- $T$  region<sup>68</sup>.

Because DAC has significantly larger thermal mass in comparison with the mass of the sample, this is practically impossible to extract the contribution of the sample in the total  $C_p(T)$  from experimental measurements of the total heat capacity. Thus, to extract the Debye

temperature for samples in DAC, temperature dependent resistive measurements are fitted to the Eq. 4.

In Figures 2 we showed the  $R(T, P = 98 \text{ GPa})$  curves and data fits to Eq. 4 for four datasets reported by Cross *et al*<sup>44</sup>.

$$R(T) = \frac{1}{\frac{1}{R_{\text{sat}}} + \frac{\theta(T_c - T) \times \left( \frac{R_n}{I_0^2 \left( C \times \left| 1 - \frac{T}{T_c} \right|^{1.5} \right)} \right) + \theta(T - T_c) \times \left( R_n - A \times \left( \frac{T_c}{\Theta_D} \right)^5 \times \int_0^{\frac{\Theta_D}{T_c}} \frac{x^5}{(e^x - 1)(1 - e^{-x})} dx - \left( \frac{T}{\Theta_D} \right)^5 \times \int_0^{\frac{\Theta_D}{T}} \frac{x^5}{(e^x - 1)(1 - e^{-x})} dx \right)} } \quad (8)$$

where  $C$  is free-fitting parameters,  $\theta(x)$  is the Heaviside step function, and  $I_0(x)$  is the zero-order modified Bessel function of the first kind.

Derived Debye temperature,  $445 \text{ K} \leq \Theta_D \leq 583 \text{ K}$ , is significantly lower than the values of  $1310 \text{ K} \leq \Theta_D \leq 1675 \text{ K}$  determined for the  $\text{LaH}_{10}$  phase, which has  $T_c > 200 \text{ K}$ <sup>53</sup>.

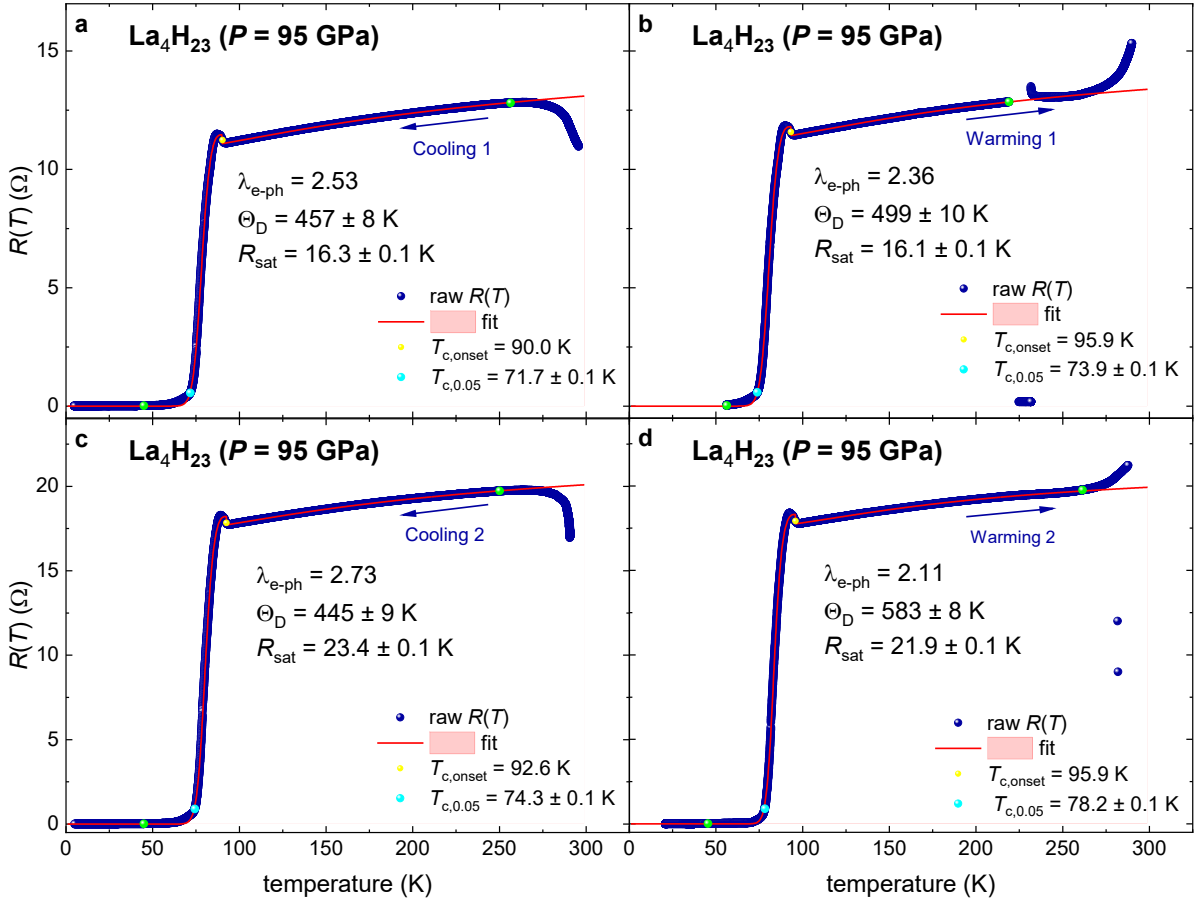


**Figure 2.** Temperature dependent resistance,  $R(T, P=98 \text{ GPa})$ , measured in compressed  $\text{La}_4\text{H}_{23}$  and data fits to Eq. 4 (raw data reported by Cross *et al*<sup>44</sup>). 95% confidence bands are shown by pink areas. Green balls indicate the bounds for which  $R(T)$  data was used for the fit to Eq. 8. Yellow balls indicate  $T_{\text{c,onset}}$ . Cyan balls indicate  $T_{\text{c},0.05}$ . Fit quality for all panels is better or equal to 0.9997. (a) – cooling 1; (b) – warming 1; (c) – cooling 2; (d) – warming 2.



However, surprisingly enough, we found that the sample designated by Drozdov *et al*<sup>39</sup> as  $\text{LaH}_{x>3}$  (compressed at pressure  $P = 150 \text{ GPa}$  and it has designation of Sample 11<sup>39</sup>) exhibits very close Debye temperature  $\Theta_D = 658 \pm 2 \text{ K}$  and  $T_{c,0.05} = 66 \text{ K}$  (Figure 3).

We have got even more surprise when we fitted to Eq. 8 the  $R(T)$  data reported by Sakata *et al*<sup>41</sup> for  $\text{LaH}_{x<10}$  (compressed at pressure  $P = 170 \text{ GPa}$ ) in their Figure 3<sup>41</sup>. We showed the  $R(T)$  data and fit in Figure 4, where one can see that the deduced  $\Theta_D = 524 \pm 24 \text{ K}$  is practically undistinguishable from the  $\Theta_D$  values deduced for four samples of the  $\text{La}_4\text{H}_{23}$  phase synthesized by Cross *et al*<sup>44</sup> (Figure 2).

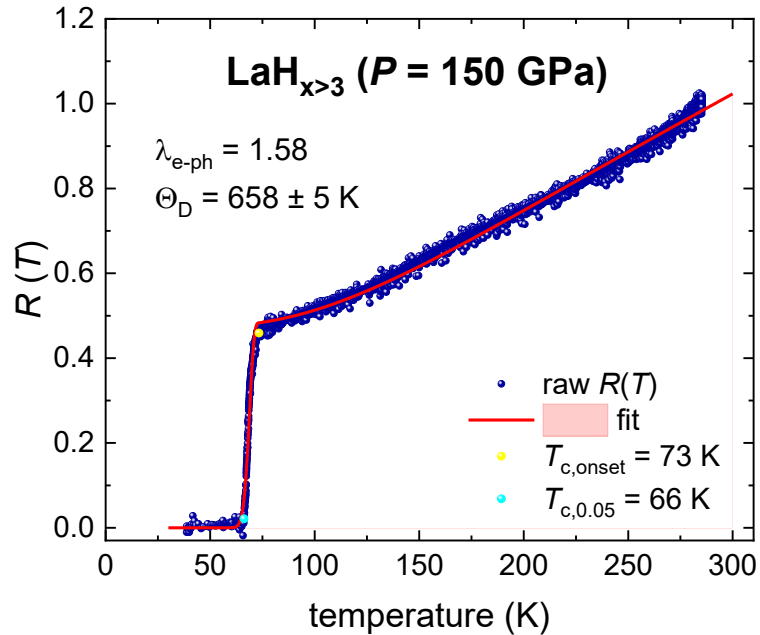


**Figure 3.** Temperature dependent resistance,  $R(T, P=150 \text{ GPa})$ , measured in compressed  $\text{LaH}_x$  ( $x > 3$ ) sample and data fit to Eq. 8 (raw data reported by Drozdov *et al*<sup>39</sup>, and this sample was designated as Sample 11 by Drozdov *et al*<sup>39</sup>). Pink area shows 95% confidence band. Yellow balls indicate  $T_{c,onset}$ . Cyan balls indicate  $T_{c,0.05}$ . Fit quality is 0.9965.

It should be noted that the  $R(T)$  curve for sample showed in Figure 4 does not reach the zero resistance, we fitted the  $R(T)$  curve to Eq. S1.

Based on results showed in Figures 3,4 we can propose that it is quite possible, that the Sample 11 reported by Drozdov *et al*<sup>39</sup> and the sample showed in Figure 3 by Sakata *et al*<sup>41</sup> are *de facto* first synthesized and studied samples of the  $\text{La}_4\text{H}_{23}$  phase in the literature.

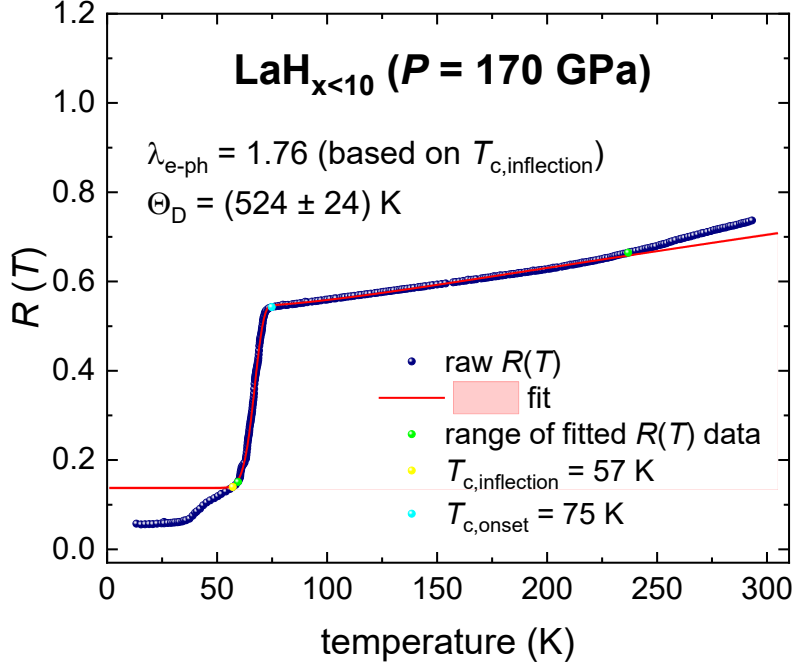


**Figure 4.** Temperature dependent resistance,  $R(T, P=170 \text{ GPa})$ , measured in compressed  $\text{LaH}_x$  ( $x < 10$ ) sample and data fit to Eq. 8 (raw data reported by Sakata *et al*<sup>41</sup> in their Figure 3). Pink area shows 95% confidence band. Yellow balls indicate  $T_{c,inflection} = 57 \text{ K}$ . Cyan balls indicate  $T_{c,onset} = 75 \text{ K}$ . Fit quality is 0.9994.

### 3.1.3. The electron phonon coupling constant

From deduced  $\Theta_D$  and extracted  $T_{c,0.05}$ , which we defined by the criterion:

$$\frac{|R(T) - R(T_{c,onset})|}{R(T_{c,onset})} = 0.05, \quad (9)$$

the electron-phonon coupling constant,  $\lambda_{e-ph}$ , can be determined as the root of advanced

McMillan equation<sup>53</sup>:

$$T_c = \left(\frac{1}{1.45}\right) \times \Theta_D \times e^{-\left(\frac{1.04(1+\lambda_{e-ph})}{\lambda_{e-ph} - \mu^*(1+0.62\lambda_{e-ph})}\right)} \times f_1 \times f_2^*, \quad (10)$$

where

$$f_1 = \left(1 + \left(\frac{\lambda_{e-ph}}{2.46(1+3.8\mu^*)}\right)^{3/2}\right)^{1/3}, \quad (11)$$

$$f_2^* = 1 + (0.0241 - 0.0735 \times \mu^*) \times \lambda_{e-ph}^2, \quad (12)$$

where  $\mu^*$  is the Coulomb pseudopotential. In this work, we fixed  $\mu^* \equiv 0.13$ , because this is a typical value for highly compressed electron-phonon mediated superconductors<sup>69-71</sup>.

Derived  $\lambda_{e-ph}$  values for the LaH<sub>x</sub> samples are shown in Figs. 2-4, where for Figure 4, the transition temperature was assumed to be the  $R(T)$  inflection temperature.

### 3.1.4. The ground state upper critical field

We deduced the upper critical field,  $B_{c2}(T)$ , from  $R(T, B)$  data reported in Fig. 3 of Ref.<sup>44</sup>.

We defined the  $B_{c2}(T)$  data by the criterion described by Eq. 9.

The deduced  $B_{c2}(T)$  dataset (Figure 5) was fitted to the analytical approximation of the Werthamer-Helfand-Hohenberg model<sup>72,73</sup>, which was proposed by Baumgartner *et al*<sup>74</sup>:

$$B_{c2}(T) = \frac{1}{0.693} \times \frac{\phi_0}{2\pi\xi^2(0)} \times \left( \left(1 - \frac{T}{T_c}\right) - 0.153 \times \left(1 - \frac{T}{T_c}\right)^2 - 0.152 \times \left(1 - \frac{T}{T_c}\right)^4 \right) \quad (13)$$

where  $\phi_0 = \frac{h}{2e}$  is the superconducting flux quantum,  $h = 6.626 \times 10^{-34} \text{ J} \cdot \text{s}$  is Planck constant,  $e = 1.602 \times 10^{-19} \text{ C}$ , and  $\xi(0)$  and  $T_c \equiv T_{c,0.05}(B = 0)$  are free fitting parameters.

The derived  $\xi(0) = 2.1 \pm 0.1 \text{ nm}$  value was used to calculate the Fermi temperature,  $T_F$ , of the La<sub>4</sub>Hi<sub>23</sub> phase.

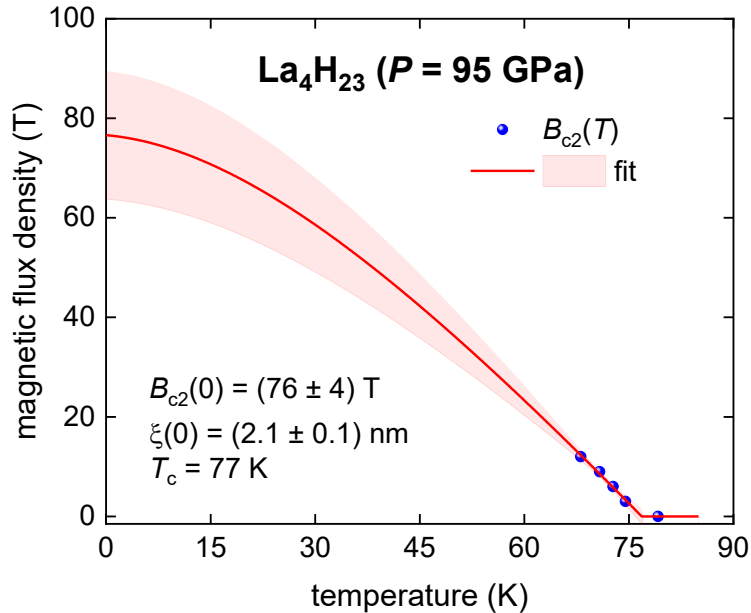


**Figure 5.** The upper critical field data,  $B_{c2}(T)$ , for compressed La<sub>4</sub>H<sub>23</sub> ( $P = 95 \text{ GPa}$ ) and data fits to Eq. 12 (raw data reported by Cross *et al*<sup>44</sup>). Pink area shows 95% confidence band.

### 3.1.5. The Fermi temperature and related ratios

To calculate the Fermi temperature, we utilized the equation<sup>75,76</sup>:

$$T_F = \frac{\pi^2 m_e}{8 \cdot k_B} \times (1 + \lambda_{e-ph}) \times \xi^2(0) \times \left( \frac{\alpha \times k_B \times T_c}{\hbar} \right)^2, \quad (14)$$

where  $m_e = 9.109 \times 10^{-31} \text{ kg}$  is bare electron mass,  $\hbar = 1.055 \times 10^{-34} \text{ J} \cdot \text{s}$  is reduced Planck constant,  $k_B = 1.381 \times 10^{-23} \text{ m}^2 \cdot \text{kg} \cdot \text{s}^{-2} \cdot \text{K}^{-1}$  is Boltzmann constant,  $\alpha \equiv \frac{2 \times \Delta(0)}{k_B \times T_c}$  is the gap-to-transition temperature ratio, where  $\Delta(0)$  is the ground state amplitude of the superconducting gap.

In Sections 3.1.2.-3.1.4. we determined all terms in the Eq. 14, except the  $\alpha \equiv \frac{2 \times \Delta(0)}{k_B \times T_c}$  value.

This value can be estimated by the linear empirical relation proposed in Ref.<sup>77</sup>:

$$\alpha \equiv \frac{2\Delta(0)}{k_B \cdot T_c} = 3.26 + 0.74 \times \lambda_{e-ph} \quad (15)$$

Considering that the free-fitting value of  $T_{c,0.05} = 77 \text{ K}$  in Fig. 5 is close to the observed  $T_{c,0.05} = 78.2 \pm 0.1 \text{ K}$  value in Figure 3,d, we substituted the derived  $\lambda_{e-ph} = 2.11$  for this sample (i.e. Fig. 3,d) in the Eq. 15, and calculated  $\alpha_{La_4H_{23}} = 4.82$ .

In the result, we estimated the  $T_F(95 \text{ GPa}) = 2.64 \times 10^3 \text{ K}$  in the  $\text{La}_4\text{H}_{23}$  ( $P = 95 \text{ GPa}$ ). It should be noted that our calculated the Fermi velocity,  $v_F(95 \text{ GPa}) = 1.60 \times 10^5 \frac{\text{m}}{\text{s}}$ , is in remarkable agreement with the value  $v_F(95 \text{ GPa}) = 1.80 \times 10^5 \frac{\text{m}}{\text{s}}$  reported by Cross *et al*<sup>44</sup>.

In the result, the  $\text{La}_4\text{H}_{23}$  ( $P = 95 \text{ GPa}$ ) falls to the unconventional superconductors band in the Uemura plot (Figure 6), and it locates near cuprates and  $\text{LaBeH}_8$  ( $P = 120 \text{ GPa}$ ) superconductor.

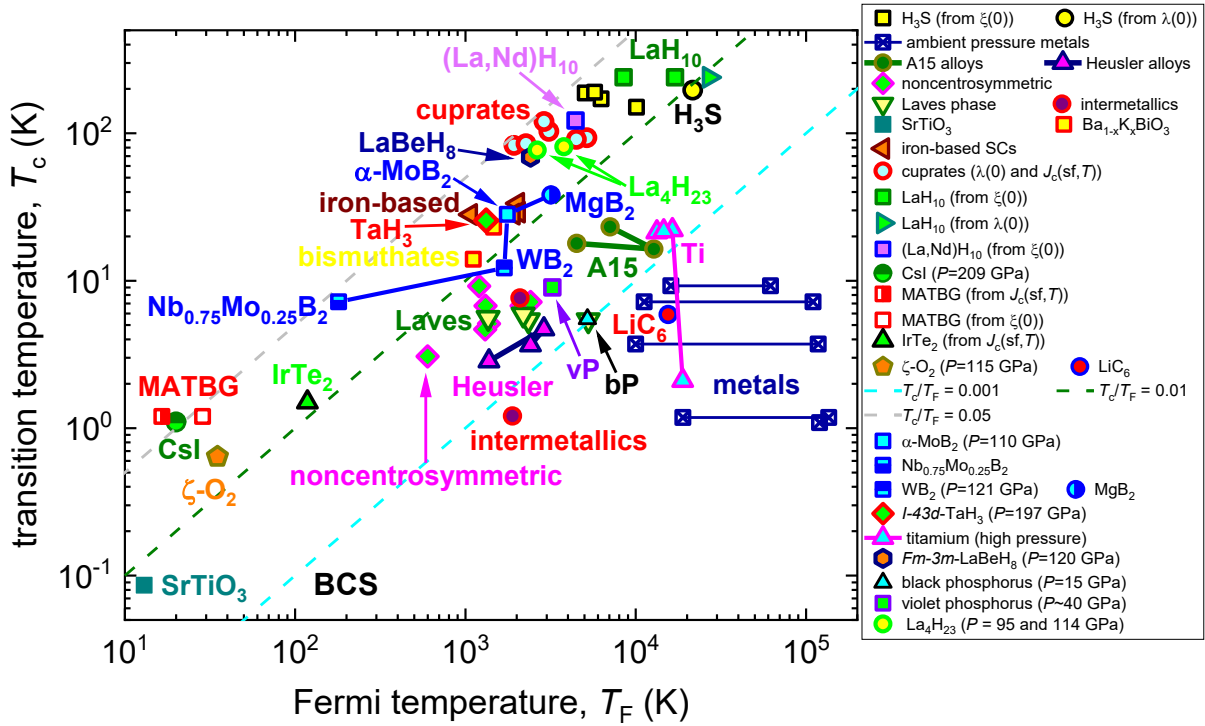


**Figure 6.** Uemura plot where the highly compressed  $La_4H_{23}$  phase is shown together with the main families of superconductors: metals, iron-based superconductors, diborides, cuprates, Laves phases, and near-room-temperature superconducting. References to original data can be found in Refs. 51,75,76,78–88

We also deduced the ratio of  $\frac{\Theta_D}{T_F}$  (95 GPa) = 0.221 for the  $La_4H_{23}$  phase. This value is used to locate this phase in the  $\frac{\Theta_D}{T_F}$  vs  $\lambda_{e-ph}$  diagram (Figure 7) (this type of diagram proposed by Pietronero *et al* <sup>84,85,89,90</sup>).

In addition, the derived ratio of  $\frac{\Theta_D}{T_F}$  (95 GPa) = 0.221 is used to locate the position of the  $La_4H_{23}$  phase in the  $\frac{\Theta_D}{T_F}$  vs  $T_c$  diagram (Figure 8) (this type of diagram proposed in Ref. <sup>78,82</sup>).

The advantage of this type of plot is that it links three primary thermodynamic quantities in superconductors, which are average energies per particles in the superconductor: the Cooper pairs, electrons, and atomic ions, while the Uemura plot (Figure 6) and the Pietronero plot (Figure 7) link only two primary energies per particles in superconductors. All values (and references, for each value) showed in Figures 6-8 are given in Refs. <sup>78,80,82</sup>.

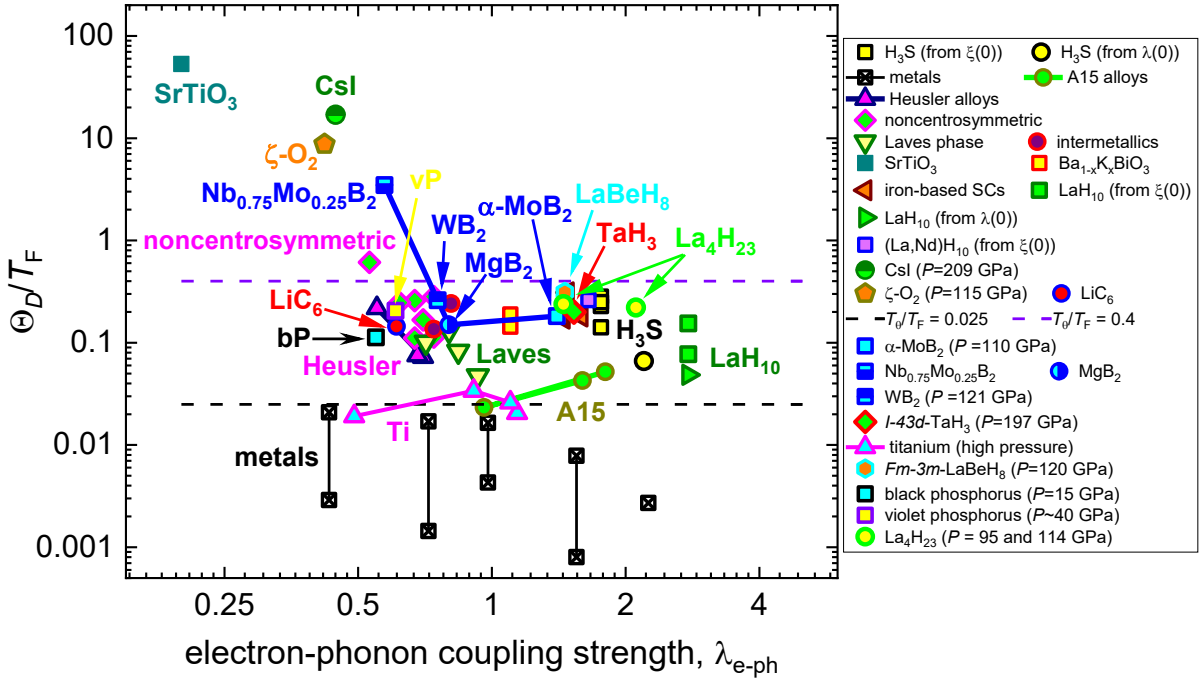


**Figure 7.** The  $\frac{\Theta_D}{T_F}$  vs  $\lambda_{e-ph}$  plot (this type of plot was proposed in Refs. <sup>84,85,89,90</sup>) where several families of superconductors and the  $La_4H_{23}$  phase. References are given in Refs. <sup>51,75,76,78–88</sup>.

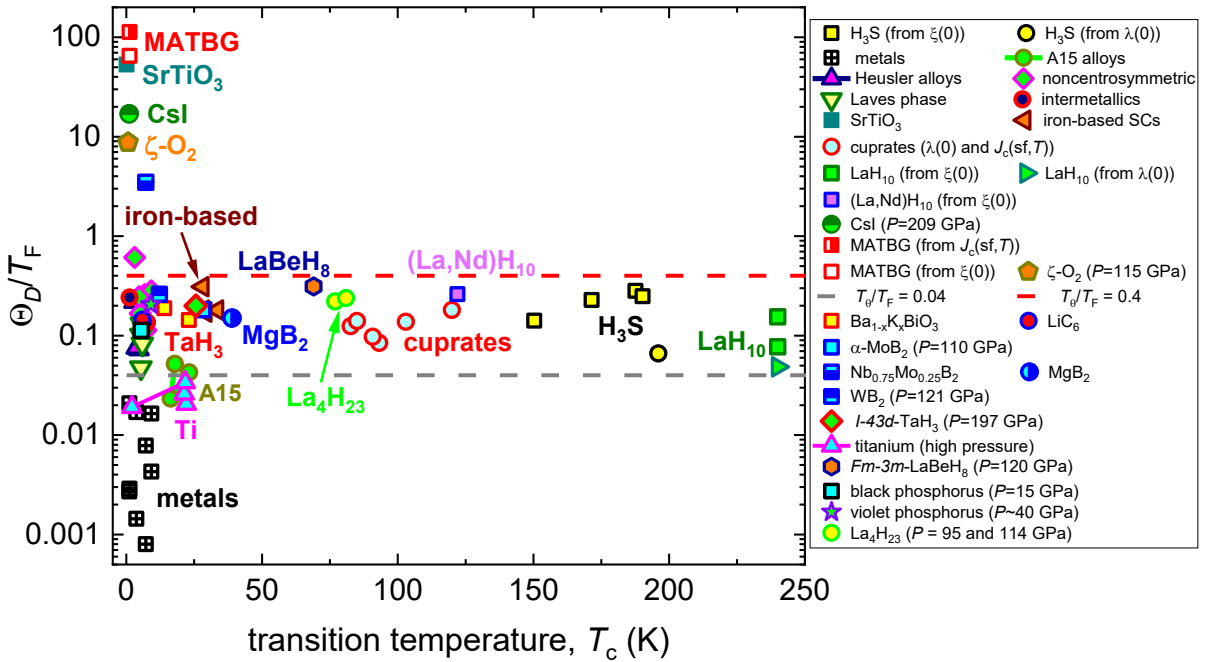


**Figure 8.** The  $\frac{\Theta_D}{T_F}$  vs  $T_c$  plot (this type of plot was proposed in Refs. <sup>78,82</sup>) for several families of superconductors and highly compressed  $La_4H_{23}$ . References are given in <sup>51,75,76,78–88</sup>.

As one can see in Figure 8, all superconductors with  $T_c \geq 20$  K exhibit the  $\frac{\Theta_D}{T_F}$  ratio within a narrow range,  $0.04 \leq \frac{\Theta_D}{T_F} \leq 0.4$ .

## 3.2. La<sub>4</sub>H<sub>23</sub> ( $P = 114$ GPa and 118 GPa)

### 3.2.1. Size-strain analysis

In Figure S2 we showed the fits of the XRD data reported by Guo *et al*<sup>43</sup> to Eq. 2. From Figure S2 one can conclude that there are many peaks which are not designated as peaks of the molybdenum and the La<sub>4</sub>H<sub>23</sub> phase (see, for instance, Figure 2 in Ref. Guo *et al*<sup>43</sup>). Thus, the Figure S2 is another confirmation of the result reported by Laniel *et al*<sup>42</sup>, that there are several La-H phases which can exist simultaneously in the La-H samples at high-pressure conditions.

In Figure 9 we show the WH analysis for the La<sub>4</sub>H<sub>23</sub> (118 GPa) sample, from which we deduced a negative value for the crystalline strain  $\varepsilon(118 \text{ GPa}) = -0.003 \pm 0.003$  (Figure 9,a).

Negative value for the strain is not the value which is often reported, however, this is not really unusual<sup>91</sup>, and, as a rule, the  $\varepsilon < 0$  values are interpreted as the absence of the strain in the crystal<sup>91</sup>. Considering that the uncertainty amplitude of the deduced  $\varepsilon$  value is the same as the amplitude of the value itself, we concluded that the sample synthesised and studied by Guo *et al*<sup>43</sup> has very low or no strain at the nanoscale.

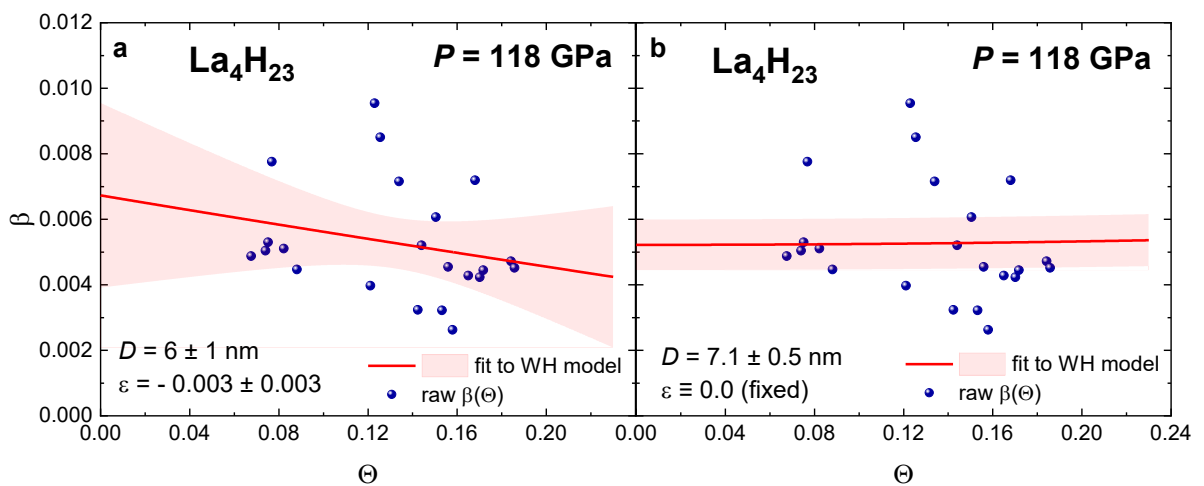


**Figure 9.** XRD peaks breadth,  $\beta(\theta)$ , and data fits to the Williamson-Hall equation (Eq. 3) for highly compressed single crystal La<sub>4</sub>H<sub>23</sub> ( $P = 118$  GPa). Raw XRD scans reported by Guo *et al*<sup>43</sup>. Pink area shows 95% confidence band. (a)  $\beta(\theta, P)$  data fit to Eq. 3 when  $D(P)$  and  $\varepsilon(P)$  are free-fitting parameters. (b)  $\beta(\theta, P)$  data fit to Eq. 3 for the condition  $\varepsilon(P) \equiv 0$ .

If so, then we can determine (with better accuracy) the grain size,  $D(118 \text{ GPa})$ , of this sample by performing the data fit to Eq. 3 at the condition of  $\varepsilon \equiv 0$ . This fit is shown in Figure 9(b), where the deduced  $D(118 \text{ GPa}) = 7.1 \pm 0.5 \text{ nm}$ . Considering that the lattice parameter  $a(118 \text{ GPa}) = 0.614 \text{ nm}$ , we can conclude that this sample has nanogranular structure  $D(118 \text{ GPa}) = (12 \pm 1) \times a$ .

### 3.2.2. Debye temperature and the electron-phonon coupling constant

The fit of the reported  $R(T)$  curve measured in the  $\text{La}_4\text{H}_{23}$  ( $114 \text{ GPa}$ ) sample by Guo *et al*<sup>43</sup> is shown in Figure 10. Derived values are  $\Theta_D(114 \text{ GPa}) = 904 \pm 69 \text{ K}$  and  $\lambda_{e-ph}(114 \text{ GPa}) = 1.45 \pm 0.08$ . The latter value was deduced for the transition temperature defined by Eq. 9. The latter value is in a good agreement with the FPC values calculated by Guo *et al*<sup>43</sup>:  $\lambda_{e-ph}(100 \text{ GPa}) = 1.49$  and  $\lambda_{e-ph}(150 \text{ GPa}) = 1.0$ .

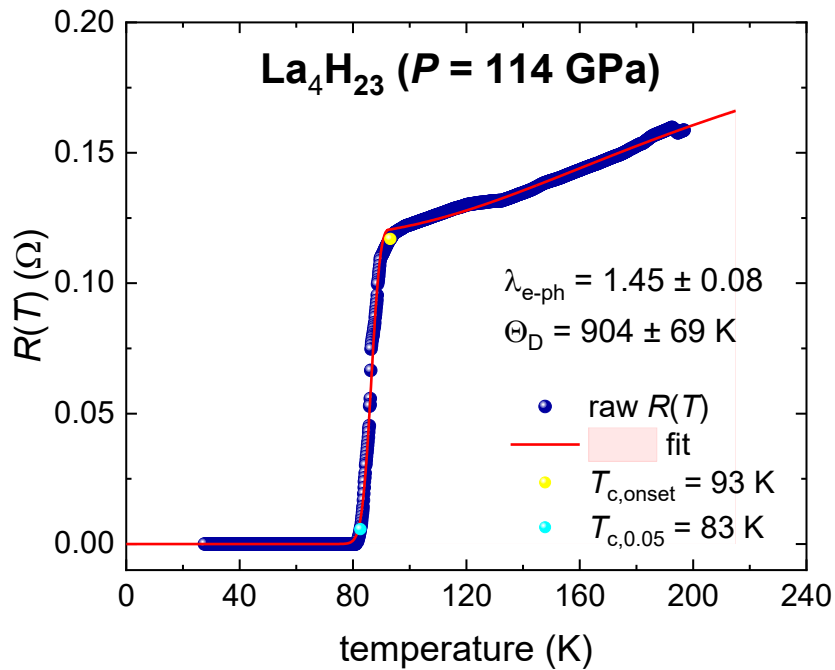


**Figure 10.** Temperature dependent resistance,  $R(T, P=114 \text{ GPa})$ , measured in compressed  $\text{La}_4\text{H}_{23}$  and data fits to Eq. 8 (raw data reported by Guo *et al*<sup>43</sup>). 95% confidence band is shown by pink area. Yellow ball indicates  $T_{c,onset}$ . Cyan ball indicates  $T_{c,0.05}$ . Fit quality is 0.9991.



### 3.2.3. The Fermi temperature and the nonadiabaticity strength constant

The ground state coherence length,  $\xi(T \rightarrow 0 K, P = 114 GPa) = 3.0 \pm 0.1 nm$ , was deduced by the fit of the  $B_{c2}(T)$  dataset to Eq.12 (see Figure 11). The  $B_{c2}(T)$  dataset was extracted from the  $R(T, B, P = 114 GPa)$  curves reported by Guo *et al*<sup>43</sup> (in their Figure 1,e<sup>43</sup>) by applying Eq. 13 criterion.

Deduced values were substituted in Eqs. 14,15 and the derived Fermi temperature is  $T_F(114 GPa) = 3800 K$ , which implies that in the Uemura plot (Fig. 6), the  $La_4H_{23}$  ( $P = 114 GPa$ ) phase falls to an unconventional superconductors band.

The ratio of  $\frac{\Theta_D}{T_F}(114 GPa) = 0.238$  which is practically undistinguishable from the  $\frac{\Theta_D}{T_F}(95 GPa) = 0.221$  and, thus, in Figure 8 the  $La_4H_{23}$  phase at two different pressures is located near each other.

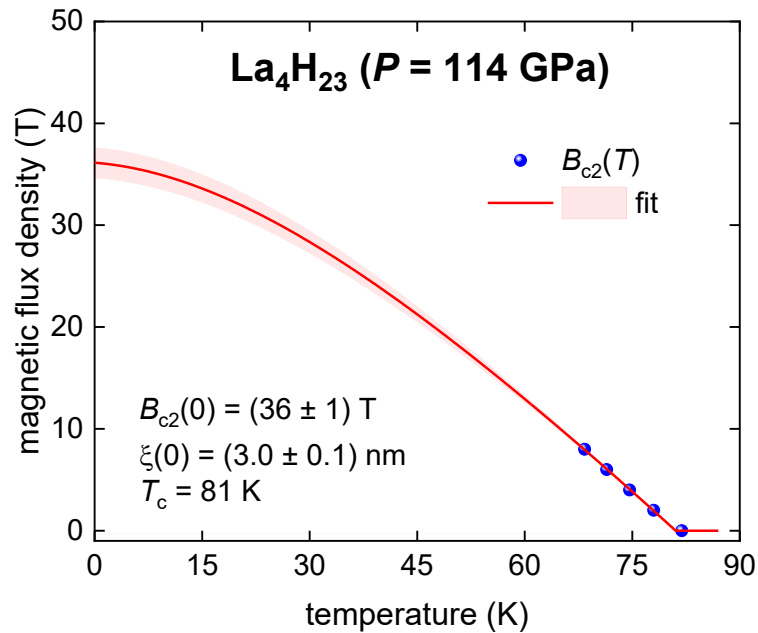


**Figure 11.** The upper critical field data,  $B_{c2}(T)$ , for compressed  $La_4H_{23}$  ( $P = 114 GPa$ ) and data fits to Eq. 12 (raw data reported by Guo *et al*<sup>43</sup>). 95% confidence band is shown by pink area.

## IV. Discussion

As we already mentioned above, the most interesting finding in our study is the fact that the  $La_4H_{23}$  phase falls to the narrow band of all superconductors with  $T_c \geq 20 K$  which

exhibit the  $\frac{\Theta_D}{T_F}$  ratio within a narrow range,  $0.04 \leq \frac{\Theta_D}{T_F} \leq 0.4$  (Figure 8). While Pietronero and co-workers<sup>84,85,89,90,92,93</sup> prefer to use the value of  $\lambda_{e-ph} \times \frac{\Theta_D}{T_F}$ , as it showed in their Figure 7<sup>84</sup>, the use of the  $\frac{\Theta_D}{T_F}$  ratio, without additional multiplication term  $\lambda_{e-ph}$ , is also useful, because it utilizes only three fundamental temperatures of any conductor, and it does not use any multiplicative factor associated with any pairing mechanism (for instance, the electron-phonon coupling strength, for the electron-phonon mediated mechanism).

Despite there is no strict theoretical explanation for this newly discovered empirical fact<sup>78,82</sup> yet, the primary physics behind this observation is more likely related to the issue that high superconducting transition temperature,  $T_c$ , emerges in materials where the highest energy of the charge carriers exceeds, but not overwhelming, the energy of the coherent oscillations of the crystalline lattice. At this condition (if even in some materials the pairing of the Cooper pairs originates from different from the electron-phonon mechanism, for instance, in cuprates), the Cooper pairs are not disturbed by either very energetic coherent lattice oscillations (in cases of  $T_F \ll \Theta_D$ ), or by uncorrelated random thermodynamic local distortions/fluctuations, which exist at high temperature in materials with low Debye temperature,  $\Theta_D \ll T_F$ .

Based on this picture, we can describe the physics behind the Uemura plot<sup>86,87,94</sup>, as an alternative presentation of the same physical picture, where however, the third fundamental temperature of any superconductor, i.e. the Debye temperature, is missed.

In this regard, our empirical finding<sup>51,52,75,76,78,79,82,95-97</sup> that all highly compressed superhydrides fall to unconventional superconductors band in the Uemura plot (despite all these superconductors exhibit the electron-phonon pairing mechanism) and which was interpreted<sup>51,52,75,76,78,79,82,95-97</sup> as the evidence for the unconventional pairing mechanism in

the superhydrides, in fact reveals the issue that the  $\frac{\Theta_D}{T_F}$  ratio for all high-temperature superconductors,  $T_c \geq 20 K$ , falls to a narrow range of  $0.04 \leq \frac{\Theta_D}{T_F} \leq 0.4$ .

Following recent theoretical understanding of the physics in superhydrides and other high-temperature superconductors<sup>84</sup> we can characterize all superhydrides by:

1. highest Debye phonon frequency,  $\omega_D \gtrsim 50 THz$ , among all superconducting materials;
2. high electron phonon coupling constant,  $\lambda_{e-ph} \gtrsim 1.5$ ;
3. reasonably high, but not record high, Fermi temperature,  $2,000 K \lesssim T_F \lesssim 30,000 K$ ;
4. significant quantum lattice fluctuations<sup>98-101</sup>, due to high frequency for the lattice oscillations associated with the lightest chemical element;
5. the presence of a Van Hove singularity close to the Fermi level;
6. moderate level of the nonadiabaticity,  $0.05 \lesssim \lambda_{e-ph} \times \frac{T_D}{T_F} \lesssim 1.0$ ;
7. reasonably high  $\frac{T_c}{T_F}$  ratio,  $0.005 \leq \frac{T_c}{T_F} \leq 0.04$ , which implies that in the Uemura plot all superhydrides fall to unconventional superconductors band.

As one can see from #1-#7 above, all electron-phonon mediated hydride superconductors have many properties which are similar or identical to cuprates and pnictides. Thus, from this point of view, all superhydrides can be classified as unconventional superconductors<sup>52,75,76,79,84,96</sup>, despite a fact that these superconductors exhibit electron-phonon pairing mechanism (which is clearly demonstrated by prominent isotope effect in direct experiments<sup>38,39</sup>).

This paradoxical understanding is clearly expressed and explained by Cappelluti et al<sup>84</sup> now, while the first presentation of this theoretical idea had been done by Luciano Pietronero at the conference in May 2017<sup>102</sup>. In peer-review form<sup>75,76</sup> (see also<sup>103</sup>) and independently this

paradox was first reported as empirical finding derived from the experimental data analysis for the temperature dependent upper critical field.

From our point of view, all mentioned above properties for high- and near-room-temperature superconductors (including cuprates, pnictides, diborides, and hydrides) can be summarized in the empirical finding condition, where three fundamental temperatures of any superconductor are obeying the strict condition<sup>78,82</sup>:

$$T_c \geq 20 \text{ K} \Rightarrow 0.04 \leq \frac{\Theta_D}{T_F} \leq 0.4 \quad (16)$$

Perhaps one of the directions for theoreticians in condensed matter physics is to find the explanation for this experimental fact (which is shown in Figure 8). It should be also noted that this understanding/explanation might lie beyond the conventional first-principles calculation studies which is the dominant theoretical approach utilized in modern high-pressure superconductivity<sup>43,69,98,104–130</sup> and global view on high-pressure superconductivity, where will be presented hydrides<sup>38,39,41–43,46,79,85,95,97–102,104,106–112,115,117,119,120,122–127,129–181</sup>, other high-pressure superconductors<sup>48,52,80,81,182–209</sup> and ambient pressure superconductors<sup>57,61,210–247</sup>, including amorphous<sup>248–250</sup> and quasicrystals<sup>251–256</sup> would be considered from the unified theoretical concept.

## V. Conclusions

In this work, we analyzed experimental data reported for highly compressed high-temperature superconducting La<sub>4</sub>H<sub>23</sub> phase. This phase is a new A-15-type phase which simultaneously extends the family of highly pressurized hydrides, the family of A-15 superconductors, and the family of high-pressure superconductors.

We found a good agreement between derived Debye temperature  $\Theta_D$  for the La<sub>4</sub>H<sub>23</sub> phase and the  $\Theta_D$  deduced for two samples with similar values of  $T_c \sim 70$  K a phase reported by Drozdov *et al*<sup>39</sup> as the unknown phase with an approximate stoichiometry of LaH<sub>x</sub> ( $x > 3$ ) and

by Sakata *et al*<sup>41</sup>, who designated the sample stoichiometry as the LaH<sub>x</sub> (x<10). From this, we proposed that *de facto* the La<sub>4</sub>H<sub>23</sub> phase was first discovered in the experiment by Drozdov *et al*<sup>39</sup> and by Sakata *et al*<sup>41</sup>.

We also found that the La<sub>4</sub>H<sub>23</sub> phase synthesised and studied by both research groups<sup>43,44</sup> has nanoscale grain size and is very low, or even the absence, of the crystalline strain.

In addition, we also deduced the values:

$$(1) 0.021 \leq \frac{T_c}{T_F} \leq 0.029;$$

$$(2) 0.22 \leq \frac{\Theta_D}{T_F} \leq 0.24;$$

$$(3) 1.5 \leq \lambda_{e-ph} \leq 2.7.$$

### **Acknowledgement**

The authors thank financial support provided by the Ministry of Science and Higher Education of Russia (theme “Pressure” No. 122021000032-5, and theme “Spin” No. 122021000036-3). Both authors gratefully acknowledged the research funding from the Ministry of Science and Higher Education of the Russian Federation under Ural Federal University Program of Development within the Priority-2030 Program.

### **The author contributions**

EFT conceived the work. EFT and VVC jointly performed data analysis and prepared figures, except 5-7 which were prepared by EFT, EFT wrote the manuscript.

### **Data availability statement**

The data that supports the findings of this study are available from the corresponding author upon reasonable request.

## Declaration of interests

The authors declare that they have no known competing financial interests or personal relationships that could have appeared to influence the work reported in this paper.

## References

1. Hardy, G. F. & Hulm, J. K. Superconducting Silicides and Germanides. *Physical Review* **89**, 884–884 (1953).
2. Dew-Hughes, D. Superconducting A-15 compounds: A review. *Cryogenics (Guildf)* **15**, 435–454 (1975).
3. Gavaler, J. R. Superconductivity in Nb–Ge films above 22 K. *Appl Phys Lett* **23**, 480–482 (1973).
4. Foner, S., McNiff, E. J., Gavaler, J. R. & Janocko, M. A. Upper critical fields of Nb<sub>3</sub>Ge thin film superconductors. *Phys Lett A* **47**, 485–486 (1974).
5. Strait, E. J. *et al.* Progress in disruption prevention for ITER. *Nuclear Fusion* **59**, 112012 (2019).
6. Mitchell, N., Breschi, M. & Tronza, V. The use of Nb 3 Sn in fusion: lessons learned from the ITER production including options for management of performance degradation. *Supercond Sci Technol* **33**, 054007 (2020).
7. Tronza, V. I. *et al.* Test results of RF ITER TF conductors in the SULTAN test facility. *IEEE Transactions on Applied Superconductivity* **24**, 1–5 (2014).
8. Ballarino, A. & Bottura, L. Targets for RandD on Nb<sub>3</sub>Sn conductor for high energy physics. *IEEE Transactions on Applied Superconductivity* **25**, 1–6 (2015).
9. Ambrosio, G. Nb<sub>3</sub>Sn High Field Magnets for the High Luminosity LHC Upgrade Project. *IEEE Transactions on Applied Superconductivity* **25**, 1–7 (2015).
10. Rochester, J., Ortino, M., Xu, X., Peng, X. & Sumption, M. The Roles of Grain Boundary Refinement and Nano-Precipitates in Flux Pinning of APC Nb<sub>3</sub>Sn. *IEEE Transactions on Applied Superconductivity* **31**, 1–5 (2021).
11. Pfeiffer, S. *et al.* Analysis of inhomogeneities in Nb<sub>3</sub>Sn wires by combined SEM and SHPM and their impact on J<sub>c</sub> and T<sub>c</sub>. *Supercond Sci Technol* **36**, 045008 (2023).
12. Senatore, C., Bagni, T., Ferradas-Troitino, J., Bordini, B. & Ballarino, A. Degradation of I<sub>c</sub> due to residual stress in high-performance Nb<sub>3</sub>Sn wires submitted to compressive transverse force. *Supercond Sci Technol* **36**, 075001 (2023).
13. Xu, X. *et al.* Significant reduction in the low-field magnetization of Nb<sub>3</sub>Sn superconducting strands using the internal oxidation APC approach. *Supercond Sci Technol* **36**, 085008 (2023).
14. Cheggour, N., Stauffer, T. C., Starch, W., Goodrich, L. F. & Splett, J. D. Implications of the strain irreversibility cliff on the fabrication of particle-accelerator magnets made of restacked-rod-process Nb<sub>3</sub>Sn wires. *Sci Rep* **9**, 5466 (2019).
15. Deryagina, I., Popova, E. & Patrakov, E. Effect of Diameter of Nb<sub>3</sub>Sn-Based Internal-Tin Wires on the Structure of Superconducting Layers. *IEEE Transactions on Applied Superconductivity* **32**, 1–5 (2022).
16. Banno, N. Low-temperature superconductors: Nb<sub>3</sub>Sn, Nb<sub>3</sub>Al, and NbTi. *Superconductivity* **6**, 100047 (2023).
17. Lee, P. J. & Larbalestier, D. C. Microstructural factors important for the development of high critical current density Nb<sub>3</sub>Sn strand. *Cryogenics (Guildf)* **48**, 283–292 (2008).
18. Segal, C. *et al.* Evaluation of critical current density and residual resistance ratio limits in powder in tube Nb<sub>3</sub>Sn conductors. *Supercond Sci Technol* **29**, 1–10 (2016).
19. Flükiger, R. *et al.* Optimization of Nb<sub>3</sub>Sn and MgB<sub>2</sub> wires. *Supercond Sci Technol* **21**, 054015 (2008).
20. Rossi, L. & Bottura, L. Superconducting Magnets for Particle Accelerators. *Reviews of Accelerator Science and Technology* **05**, 51–89 (2012).
21. Godeke, A. *Performance Boundaries in Nb<sub>3</sub>Sn*. vol. PhD (PhD Thesis, University of Twente, Enschede, Netherlands, 2005).

22. Deryagina, I. L., Popova, E. N., Patrakov, E. I. & Valova-Zaharevskaya, E. G. Effect of Nb<sub>3</sub>Sn layer structure and morphology on critical current density of multifilamentary superconductors. *J Magn Magn Mater* **440**, 119–122 (2017).
23. Fischer, C. M. Investigation of the Relationships between Superconducting Properties and Nb<sub>3</sub>Sn Reaction Conditions in Powder-in-Tube Nb<sub>3</sub>Sn Conductors. (2002).
24. Uglietti, D., Abacherli, V., Cantoni, M. & Flukiger, R. Grain growth, morphology, and composition profiles in industrial Nb<sub>3</sub>Sn wires. *IEEE Transactions on Applied Superconductivity* **17**, 2615–2618 (2007).
25. Abächerli, V. *et al.* The influence of Ti doping methods on the high field performance of (Nb, Ta, Ti)<sub>3</sub>Sn multifilamentary wires using osprey bronze. *IEEE Transactions on Applied Superconductivity* **15**, 3482–3485 (2005).
26. Schauer, W. & Schelb, W. Improvement of Nb<sub>3</sub>Sn high field critical current by a two-stage reaction. *IEEE Trans Magn* **17**, 374–377 (1981).
27. Lee, P. J., Squitieri, A. A. & Larbalestier, D. C. Nb<sub>3</sub>Sn: macrostructure, microstructure, and property comparisons for bronze and internal Sn process strands. *IEEE Transactions on Applied Superconductivity* **10**, 979–982 (2000).
28. Godeke, A., den Ouden, A., Nijhuis, A. & ten Kate, H. H. J. State of the art powder-in-tube niobium–tin superconductors. *Cryogenics (Guildf)* **48**, 308–316 (2008).
29. Pong, I. *et al.* Microstructure development in Nb<sub>3</sub>Sn(Ti) internal tin superconducting wire. *J Mater Sci* **43**, 3522–3530 (2008).
30. Cantoni, M. *et al.* Sn concentration gradients in Powder-in-Tube superconductors. *J Phys Conf Ser* **234**, 022005 (2010).
31. Sanabria, C. *et al.* Controlling Cu–Sn mixing so as to enable higher critical current densities in RRP® Nb<sub>3</sub>Sn wires. *Supercond Sci Technol* **31**, 064001 (2018).
32. Barzi, E. *et al.* RRP Nb<sub>3</sub>Sn Strand Studies for LARP. *IEEE Transactions on Applied Superconductivity* **17**, 2607–2610 (2007).
33. Godeke, A. A review of the properties of Nb<sub>3</sub>Sn and their variation with A15 composition, morphology and strain state. *Supercond Sci Technol* **19**, R68–R80 (2006).
34. Tarantini, C. *et al.* Origin of the enhanced Nb<sub>3</sub>Sn performance by combined Hf and Ta doping. *Sci Rep* **11**, 17845 (2021).
35. Parrell, J. A. *et al.* Internal tin Nb<sub>3</sub>Sn conductors engineered for fusion and particle accelerator applications. *IEEE Transactions on Applied Superconductivity* **19**, 2573–2579 (2009).
36. Deryagina, I., Popova, E., Patrakov, E. & Valova-Zaharevskaya, E. Structure of superconducting layers in bronze-processed and internal-tin Nb<sub>3</sub>Sn-based wires of various designs. *J Appl Phys* **121**, 233901 (2017).
37. Talantsev, E. F., Valova-Zaharevskaya, E. G., Deryagina, I. L. & Popova, E. N. Characteristic Length for Pinning Force Density in Nb<sub>3</sub>Sn. *Materials* **16**, 5185 (2023).
38. Drozdov, A. P., Erements, M. I., Troyan, I. A., Ksenofontov, V. & Shylin, S. I. Conventional superconductivity at 203 kelvin at high pressures in the sulfur hydride system. *Nature* **525**, 73–76 (2015).
39. Drozdov, A. P. *et al.* Superconductivity at 250 K in lanthanum hydride under high pressures. *Nature* **569**, 528–531 (2019).
40. Somayazulu, M. *et al.* Evidence for Superconductivity above 260 K in Lanthanum Superhydride at Megabar Pressures. *Phys Rev Lett* **122**, 027001 (2019).
41. Sakata, M. *et al.* Superconductivity of lanthanum hydride synthesized using AIH 3 as a hydrogen source. *Supercond Sci Technol* **33**, 114004 (2020).
42. Laniel, D. *et al.* High-pressure synthesis of seven lanthanum hydrides with a significant variability of hydrogen content. *Nat Commun* **13**, 6987 (2022).
43. Guo, J. *et al.* Stabilization of high-temperature superconducting A15 phase La<sub>4</sub>H<sub>23</sub> below 100 GPa. (2023) doi:10.48550/arXiv.2307.13067.
44. Cross, S. *et al.* High-temperature superconductivity in  $\text{La}_{4-x}\text{H}_{23}$  below 100 GPa. *Phys Rev B* **109**, L020503 (2024).
45. Sanna, A., Pellegrini, C., di Cataldo, S., Profeta, G. & Boeri, L. A possible explanation for the high superconducting T<sub>c</sub> in bcc Ti at high pressure. (2023).
46. Liu, H., Liu, C., Ma, Y. & Chen, C. Prominent stress-driven anomalies in superconductivity of yttrium hexahydride. *Phys Rev B* **109**, 064513 (2024).

47. Prischepea, S. L. & Kushnir, V. N. Phonon softening in nanostructured phonon-mediated superconductors (review). *Journal of Physics: Condensed Matter* **35**, 313003 (2023).
48. Talantsev, E. F. & Chistyakov, V. V. Debye temperature, electron-phonon coupling constant, and microcrystalline strain in highly-compressed La<sub>3</sub>Ni<sub>2</sub>O<sub>7- $\delta$</sub> . (2024) doi:10.48550/arXiv.2401.00804.
49. Williamson, G. K. & Hall, W. H. X-ray line broadening from filed aluminium and wolfram. *Acta Metallurgica* **1**, 22–31 (1953).
50. Khan, M. Z. *et al.* Improved interface growth and enhanced flux pinning in YBCO films deposited on an advanced IBAD-MgO based template. *Physica C: Superconductivity and its Applications* **545**, 50–57 (2018).
51. Talantsev, E. F. Electron–phonon coupling constant and BCS ratios in LaH<sub>10-y</sub> doped with magnetic rare-earth element. *Supercond Sci Technol* **35**, 095008 (2022).
52. Talantsev, E. F. An approach to identifying unconventional superconductivity in highly-compressed superconductors. *Supercond Sci Technol* **33**, 124001 (2020).
53. Talantsev, E. F. Advanced McMillan’s equation and its application for the analysis of highly-compressed superconductors. *Supercond Sci Technol* **33**, 094009 (2020).
54. Wiesmann, H. *et al.* Simple Model for Characterizing the Electrical Resistivity in  $A_{15}$  Superconductors. *Phys Rev Lett* **38**, 782–785 (1977).
55. Talantsev, E. F. Quantifying interaction mechanism in infinite layer nickelate superconductors. *J Appl Phys* **134**, (2023).
56. Kushwaha, R. K. *et al.* Superconductivity in new family of Rhenium-based binary alloys: Re<sub>7</sub>X<sub>3</sub> (X = Nb, Ta, Ti, Zr, Hf). (2024).
57. Watanabe, Y., Miura, A., Moriyoshi, C., Yamashita, A. & Mizuguchi, Y. Observation of superconductivity and enhanced upper critical field of  $\eta$ -carbide-type oxide Zr<sub>4</sub>Pd<sub>2</sub>O. *Sci Rep* **13**, 22458 (2023).
58. Shang, T., Svanidze, E. & Shiroka, T. Probing the superconducting pairing of the La<sub>4</sub>Be<sub>33</sub>Pt<sub>16</sub> alloy via muon-spin spectroscopy. *Journal of Physics: Condensed Matter* **36**, 105601 (2024).
59. Świątek, H. *et al.* Detailed studies of superconducting properties of Y<sub>2</sub>Pd<sub>1.25</sub>Ge<sub>2.75</sub>. *J Alloys Compd* **971**, 172712 (2024).
60. Gutowska, S., Wiendlocha, B., Klimczuk, T. & Winiarski, M. J. Superconductivity in Bismuth Pyrochlore Lattice Compounds RbBi<sub>2</sub> and CsBi<sub>2</sub>: The Role of Relativistic Effects. *The Journal of Physical Chemistry C* **127**, 14402–14414 (2023).
61. Górnicka, K., Winiarski, M. J., Walicka, D. I. & Klimczuk, T. Superconductivity in a breathing kagome metals RO<sub>2</sub> (R = Sc, Y, Lu). *Sci Rep* **13**, 16704 (2023).
62. Klimczuk, T., Królak, S. & Cava, R. J. Superconductivity of Ta-Hf and Ta-Zr alloys: Potential alloys for use in superconducting devices. *Phys Rev Mater* **7**, 064802 (2023).
63. Bhattacharyya, A., Adroja, D. T., Hillier, A. D. & Biswas, P. K. Superconducting Gap Structure of Filled Skutterudite LaOs<sub>4</sub>As<sub>12</sub> Compound through  $\mu$ SR Investigations. *Magnetochemistry* **9**, 117 (2023).
64. Xiao, G. *et al.* Superconductivity and strong spin-orbit coupling in a new noncentrosymmetric compound ThIrP. *Sci China Phys Mech Astron* **64**, 107411 (2021).
65. Pallecchi, I. *et al.* Experimental investigation of electronic interactions in collapsed and uncollapsed  $\text{LaFeAs}_2$  phases. *Phys Rev B* **108**, 014512 (2023).
66. Ni, D. *et al.* Layered polymorph of titanium triiodide. *Phys Rev Mater* **6**, 124001 (2022).
67. Yang, K. *et al.* Charge fluctuations above  $T_{\text{CDW}}$  revealed by glasslike thermal transport in kagome metals  $\text{AV}_3\text{Sb}_5$  ( $A = \text{Rb}, \text{Cs}, \text{K}$ ). *Phys Rev B* **107**, 184506 (2023).
68. Jacobs, B. S. & Pandey, A.  $\text{BaMn}_2\text{P}_2$ : Highest magnetic ordering temperature 122-pnictide compound. *Phys Rev Mater* **7**, 044410 (2023).
69. Zhang, Z. *et al.* Design Principles for High-Temperature Superconductors with a Hydrogen-Based Alloy Backbone at Moderate Pressure. *Phys Rev Lett* **128**, 047001 (2022).



70. Lim, J. *et al.* Creating superconductivity in WB2 through pressure-induced metastable planar defects. *Nat Commun* **13**, 7901 (2022).
71. Hire, A. C. *et al.* High critical field superconductivity at ambient pressure in  $\text{MoB}_2$  stabilized in the P6/mmm structure via Nb substitution. *Phys Rev B* **106**, 174515 (2022).
72. Helfand, E. & Werthamer, N. R. Temperature and Purity Dependence of the Superconducting Critical Field, 
$$H_c^2 = H_c^2(0) \left( \frac{1 - T/T_c}{1 - T_c/T_c} \right)^2$$
. II. *Physical Review* **147**, 288–294 (1966).
73. Werthamer, N. R., Helfand, E. & Hohenberg, P. C. Temperature and Purity Dependence of the Superconducting Critical Field, 
$$H_c^2 = H_c^2(0) \left( \frac{1 - T/T_c}{1 - T_c/T_c} \right)^2$$
. III. Electron Spin and Spin-Orbit Effects. *Physical Review* **147**, 295–302 (1966).
74. Baumgartner, T. *et al.* Effects of neutron irradiation on pinning force scaling in state-of-the-art Nb 3 Sn wires. *Supercond Sci Technol* **27**, 015005 (2014).
75. Talantsev, E. F. Classifying hydrogen-rich superconductors. *Mater Res Express* **6**, 106002 (2019).
76. Talantsev, E. F. Classifying superconductivity in compressed H3S. *Modern Physics Letters B* **33**, 1950195 (2019).
77. Talantsev, E. F. The Compliance of the Upper Critical Field in Magic-Angle Multilayer Graphene with the Pauli Limit. *Materials* **16**, 256 (2022).
78. Talantsev, E. F. Quantifying the Nonadiabaticity Strength Constant in Recently Discovered Highly Compressed Superconductors. *Symmetry (Basel)* **15**, 1632 (2023).
79. Talantsev, E. F. Comparison of highly-compressed C2/m-SnH12 superhydride with conventional superconductors. *Journal of Physics: Condensed Matter* **33**, 285601 (2021).
80. Talantsev, E. F. D-Wave Superconducting Gap Symmetry as a Model for Nb<sub>1-x</sub>MoxB<sub>2</sub> (x = 0.25; 1.0) and WB<sub>2</sub> Diborides. *Symmetry (Basel)* **15**, 812 (2023).
81. Talantsev, E. F. Fermi-Liquid Nonadiabatic Highly Compressed Cesium Iodide Superconductor. *Condens Matter* **7**, 65 (2022).
82. Talantsev, E. F. Quantifying Nonadiabaticity in Major Families of Superconductors. *Nanomaterials* **13**, 71 (2022).
83. Talantsev, E. F. The electron–phonon coupling constant and the Debye temperature in polyhydrides of thorium, hexadeuteride of yttrium, and metallic hydrogen phase III. *J Appl Phys* **130**, 195901 (2021).
84. Cappelluti, E., Grimaldi, C. & Pietronero, L. Electron–phonon driven unconventional superconductivity: The role of small Fermi energies and of nonadiabatic processes. *Physica C: Superconductivity and its Applications* **613**, 1354343 (2023).
85. Pietronero, L., Boeri, L., Cappelluti, E. & Ortenzi, L. Conventional/unconventional superconductivity in high-pressure hydrides and beyond: insights from theory and perspectives. *Quantum Studies: Mathematics and Foundations* **5**, 5–21 (2018).
86. Uemura, Y. J. Bose-Einstein to BCS crossover picture for high-T cuprates. *Physica C Supercond* **282–287**, 194–197 (1997).
87. Uemura, Y. J. Dynamic superconductivity responses in photoexcited optical conductivity and Nernst effect. *Phys Rev Mater* **3**, 104801 (2019).
88. Szcze,śniak, D. Scalability of non-adiabatic effects in lithium-decorated graphene superconductor. *Europhys Lett* **142**, 36002 (2023).
89. Cappelluti, E., Ciuchi, S., Grimaldi, C., Pietronero, L. & Strässler, S. High T<sub>c</sub> Superconductivity in MgB<sub>2</sub> by Nonadiabatic Pairing. *Phys Rev Lett* **88**, 117003 (2002).
90. Pietronero, L., Strässler, S. & Grimaldi, C. Nonadiabatic superconductivity. I. Vertex corrections for the electron-phonon interactions. *Phys Rev B* **52**, 10516–10529 (1995).
91. Langford, J. I., Cernik, R. J. & Louër, D. The breadth and shape of instrumental line profiles in high-resolution powder diffraction. *J Appl Crystallogr* **24**, 913–919 (1991).
92. Grimaldi, C., Cappelluti, E. & Pietronero, L. Isotope effect on m\* in high- T<sub>c</sub> materials due to the breakdown of Migdal’s theorem. *Europhysics Letters (EPL)* **42**, 667–672 (1998).
93. Grimaldi, C., Pietronero, L. & Strässler, S. Nonadiabatic superconductivity. II. Generalized Eliashberg equations beyond Migdal’s theorem. *Phys Rev B* **52**, 10530–10546 (1995).
94. Uemura, Y. J. *et al.* Universal Correlations between  $T_c$  and  $c$  and

- $\frac{\langle \text{mrow} \langle \text{mrow} \langle \text{msub} \langle \text{mrow} \langle \text{mi} \rangle \text{n} \rangle \rangle \rangle \rangle}{\langle \text{mrow} \langle \text{mi} \rangle \text{s} \rangle \langle \text{mi} \rangle}$ . *Phys Rev Lett* **62**, 2317–2320 (1989).
95. Talantsev, E. F. Universal Fermi velocity in highly compressed hydride superconductors. *Matter and Radiation at Extremes* **7**, 058403 (2022).
  96. Talantsev, E. F. Unconventional superconductivity in highly-compressed unannealed sulphur hydride. *Results Phys* **16**, 102993 (2020).
  97. Talantsev, E. F. & Mataira, R. C. Classifying superconductivity in ThH-ThD superhydrides/superdeuterides. *Mater Res Express* **7**, 016003 (2020).
  98. Errea, I. Superconducting hydrides on a quantum landscape. *Journal of Physics: Condensed Matter* **34**, 231501 (2022).
  99. Wang, H. *et al.* Quantum structural fluxion in superconducting lanthanum polyhydride. *Nat Commun* **14**, 1674 (2023).
  100. Errea, I. *et al.* Quantum hydrogen-bond symmetrization in the superconducting hydrogen sulfide system. *Nature* **532**, 81–84 (2016).
  101. Errea, I. *et al.* Quantum crystal structure in the 250-kelvin superconducting lanthanum hydride. *Nature* **578**, 66–69 (2020).
  102. L. Pietronero, L. Boeri, E. Cappellut & L. Ortenzi. Conventional/Unconventional superconductivity in high pressure hydrides and beyond: Insights from theory and perspectives. in *2nd International Workshop 'Towards Room Temperature Superconductivity: Superhydrides and More.'* In Recognition of Professor Vitaly Ginzburg. (eds. Organizers: *et al.*) (Orange, CA, USA, 2017).
  103. Talantsev, E. F. Classifying superconductivity in compressed H<sub>3</sub>S. (2019) doi:10.48550/arXiv.1902.01772.
  104. Durajski, A. P. & Szczęśniak, R. First-Principles Estimation of Low-Pressure Superconductivity in KC<sub>2</sub>H<sub>8</sub> Ternary Hydride. *physica status solidi (RRL) – Rapid Research Letters* **17**, (2023).
  105. Wu, Z. *et al.* Effect of doping on the phase stability and superconductivity in  $\langle \text{mrow} \langle \text{mi} \rangle \text{La} \rangle \langle \text{msub} \langle \text{mi} \text{mathvariant}=\text{"normal"} \rangle \text{H} \rangle \langle \text{mn} \rangle 10 \langle \text{mn} \rangle \langle \text{msub} \rangle \langle \text{mrow} \rangle \langle \text{mi} \rangle$ . *Phys Rev Mater* **7**, L101801 (2023).
  106. Gao, K. *et al.* Prediction of high-  $\langle \text{math} \langle \text{msub} \langle \text{mi} \rangle T \rangle \langle \text{mi} \rangle \text{c} \rangle \langle \text{msub} \rangle \langle \text{math} \rangle$  superconductivity in ternary actinium beryllium hydrides at low pressure. *Phys Rev B* **109**, 014501 (2024).
  107. Song, P. *et al.* (La,Th)H<sub>10</sub>: Potential High-  $T_c$  (242 K) Superconductors Stabilized Thermodynamically below 200 GPa. *The Journal of Physical Chemistry C* **128**, 2656–2665 (2024).
  108. Struzhkin, V. *et al.* Superconductivity in La and Y hydrides: Remaining questions to experiment and theory. *Matter and Radiation at Extremes* **5**, (2020).
  109. Troyan, I. A. *et al.* High-temperature superconductivity in hydrides. *Physics-Uspekhi* **65**, 748–761 (2022).
  110. Zhang, X., Zhao, Y. & Yang, G. Superconducting ternary hydrides under high pressure. *WIREs Computational Molecular Science* **12**, (2022).
  111. Semenok, D. V., Kruglov, I. A., Savkin, I. A., Kvashnin, A. G. & Oganov, A. R. On Distribution of Superconductivity in Metal Hydrides. *Curr Opin Solid State Mater Sci* **24**, 100808 (2020).
  112. Semenok, D. V. *et al.* Superconductivity at 253 K in lanthanum–yttrium ternary hydrides. *Materials Today* **48**, 18–28 (2021).
  113. Du, M. *et al.* High-temperature superconductivity in transition metallic hydrides MH<sub>11</sub> (M = Mo, W, Nb, and Ta) under high pressure. *Physical Chemistry Chemical Physics* **23**, 6717–6724 (2021).
  114. Du, M., Zhao, W., Cui, T. & Duan, D. Compressed superhydrides: the road to room temperature superconductivity. *Journal of Physics: Condensed Matter* **34**, 173001 (2022).
  115. Du, M., Li, Z., Duan, D. & Cui, T. Superconducting phases of YH<sub>9</sub> under pressure. *Phys Rev B* **108**, 174507 (2023).
  116. Du, M., Song, H., Zhang, Z., Duan, D. & Cui, T. Room-Temperature Superconductivity in Yb/Lu Substituted Clathrate Hexahydrides under Moderate Pressure. *Research* **2022**, (2022).
  117. Chen, W. *et al.* High-Temperature Superconducting Phases in Cerium Superhydride with a  $T_c$  up to 115 K below a Pressure of 1 Megabar. *Phys Rev Lett* **127**, 117001 (2021).
  118. Zhao, W. *et al.* Pressure Induced Clathrate Hydrogen-Rich Superconductors KH<sub>20</sub> and KH<sub>30</sub>. *Inorg Chem* **61**, 18112–18118 (2022).
  119. Duan, D. *et al.* Pressure-induced metallization of dense (H<sub>2</sub>S)<sub>2</sub>H<sub>2</sub> with high- $T_c$  superconductivity. *Sci Rep* **4**, 6968 (2014).

120. Zhou, D. *et al.* Superconducting praseodymium superhydrides. *Sci Adv* **6**, 1–9 (2020).
121. Xie, H. *et al.* Hydrogen Pentagraphenelike Structure Stabilized by Hafnium: A High-Temperature Conventional Superconductor. *Phys Rev Lett* **125**, 217001 (2020).
122. Chen, W. *et al.* Synthesis of molecular metallic barium superhydride: pseudocubic BaH<sub>12</sub>. *Nat Commun* **12**, 1–9 (2021).
123. Chen, W. *et al.* Enhancement of superconducting properties in the La–Ce–H system at moderate pressures. *Nat Commun* **14**, 2660 (2023).
124. Semenok, D. V. *et al.* Superconductivity at 161 K in thorium hydride ThH<sub>10</sub>: Synthesis and properties. *Materials Today* **33**, 36–44 (2020).
125. Troyan, I. A. *et al.* Anomalous High-Temperature Superconductivity in YH<sub>6</sub>. *Advanced Materials* **33**, 2006832 (2021).
126. Semenok, D. V. *et al.* Effect of Magnetic Impurities on Superconductivity in LaH<sub>10</sub>. *Advanced Materials* **34**, 2204038 (2022).
127. Lilia, B. *et al.* The 2021 room-temperature superconductivity roadmap. *Journal of Physics: Condensed Matter* **34**, 183002 (2022).
128. Mao, H.-K. Hydrogen and related matter in the pressure dimension. *Matter and Radiation at Extremes* **7**, 063001 (2022).
129. Ma, L. *et al.* High-Temperature Superconducting Phase in Clathrate Calcium Hydride CaH<sub>6</sub> up to 215 K at a Pressure of 172 GPa. *Phys Rev Lett* **128**, 167001 (2022).
130. Bi, J. *et al.* Stabilization of superconductive La–Y alloy superhydride with T<sub>c</sub> above 90 K at megabar pressure. *Materials Today Physics* **28**, 100840 (2022).
131. Pickard, C. J., Errea, I. & Eremets, M. I. Superconducting Hydrides Under Pressure. *Annu Rev Condens Matter Phys* **11**, 57–76 (2020).
132. Goh, S. K., Zhang, W. & Yip, K. Y. Trapped magnetic flux in superconducting hydrides. *Nat Phys* (2023) doi:10.1038/s41567-023-02101-8.
133. Heil, C., di Cataldo, S., Bachelet, G. B. & Boeri, L. Superconductivity in sodalite-like yttrium hydride clathrates. *Phys Rev B* **99**, 220502 (2019).
134. Goncharenko, I. *et al.* Pressure-Induced Hydrogen-Dominant Metallic State in Aluminum Hydride. *Phys Rev Lett* **100**, 045504 (2008).
135. Hong, F. *et al.* Possible superconductivity at ~70 K in tin hydride SnH<sub>x</sub> under high pressure. *Materials Today Physics* **22**, 100596 (2022).
136. Huang, X. *et al.* High-temperature superconductivity in sulfur hydride evidenced by alternating-current magnetic susceptibility. *Natl Sci Rev* **6**, 713–718 (2019).
137. Tongkhonburi, P., Udomsamuthirun, P., Changjan, A., Meakniti, S. & Krueahong, T. The Study on the Critical Temperature and Gap-to-T<sub>c</sub> Ratio of Yttrium Hydride Superconductors. *Crystals (Basel)* **14**, 158 (2024).
138. Sun, Y., Lv, J., Xie, Y., Liu, H. & Ma, Y. Route to a Superconducting Phase above Room Temperature in Electron-Doped Hydride Compounds under High Pressure. *Phys Rev Lett* **123**, 097001 (2019).
139. Meninno, A. & Errea, I. Ab initio study of metastable occupation of tetrahedral sites in palladium hydrides and its impact on superconductivity. *Phys Rev B* **107**, 024504 (2023).
140. Li, Y., Hao, J., Liu, H., Li, Y. & Ma, Y. The metallization and superconductivity of dense hydrogen sulfide. *J Chem Phys* **140**, (2014).
141. Wang, H., Tse, J. S., Tanaka, K., Iitaka, T. & Ma, Y. Superconductive sodalite-like clathrate calcium hydride at high pressures. *Proceedings of the National Academy of Sciences* **109**, 6463–6466 (2012).
142. Sun, D. *et al.* High-temperature superconductivity on the verge of a structural instability in lanthanum superhydride. *Nat Commun* **12**, 6863 (2021).
143. Cai, W. *et al.* Superconductivity above 180 K in Ca–Mg Ternary Superhydrides at Megabar Pressures. (2023) doi:10.48550/arXiv.2312.06090.
144. Cao, Z.-Y. *et al.* Probing superconducting gap in CeH<sub>9</sub> under pressure. (2024) doi:10.48550/arXiv.2401.12682.
145. Semenok, D. *et al.* Evidence for Pseudogap Phase in Cerium Superhydrides: CeH<sub>10</sub> and CeH<sub>9</sub>. (2023).
146. Li, Z. *et al.* Superconductivity above 200 K discovered in superhydrides of calcium. *Nat Commun* **13**, 2863 (2022).

147. Kong, P. *et al.* Superconductivity up to 243 K in the yttrium-hydrogen system under high pressure. *Nat Commun* **12**, 5075 (2021).
148. Minkov, V. S., Prakapenka, V. B., Greenberg, E. & Eremets, M. I. A Boosted Critical Temperature of 166 K in Superconducting D<sub>3</sub>S Synthesized from Elemental Sulfur and Hydrogen. *Angewandte Chemie* **132**, 19132–19136 (2020).
149. Minkov, V. S., Ksenofontov, V., Bud'ko, S. L., Talantsev, E. F. & Eremets, M. I. Magnetic flux trapping in hydrogen-rich high-temperature superconductors. *Nat Phys* (2023) doi:10.1038/s41567-023-02089-1.
150. Minkov, V. S. *et al.* Magnetic field screening in hydrogen-rich high-temperature superconductors. *Nat Commun* **13**, 3194 (2022).
151. Mozaffari, S. *et al.* Superconducting phase diagram of H<sub>3</sub>S under high magnetic fields. *Nat Commun* **10**, 2522 (2019).
152. Purans, J. *et al.* Local electronic structure rearrangements and strong anharmonicity in YH<sub>3</sub> under pressures up to 180 GPa. *Nat Commun* **12**, 1765 (2021).
153. Errea, I. *et al.* High-Pressure Hydrogen Sulfide from First Principles: A Strongly Anharmonic Phonon-Mediated Superconductor. *Phys Rev Lett* **114**, 157004 (2015).
154. He, X. *et al.* Superconductivity discovered in niobium polyhydride at high pressures. *Materials Today Physics* **40**, 101298 (2024).
155. Zhang, C. L. *et al.* Superconductivity above 80 K in polyhydrides of hafnium. *Materials Today Physics* **27**, 100826 (2022).
156. He, X. *et al.* Superconductivity Observed in Tantalum Polyhydride at High Pressure. *Chinese Physics Letters* **40**, 057404 (2023).
157. Semenok, D. Computational design of new superconducting materials and their targeted experimental synthesis. *PhD Thesis; Skolkovo Institute of Science and Technology* (2023) doi:10.13140/RG.2.2.28212.12161.
158. Sadakov, A. V. *et al.* Vortex Phase Dynamics in Yttrium Superhydride YH<sub>6</sub> at Megabar Pressures. *J Phys Chem Lett* **14**, 6666–6671 (2023).
159. Troyan, I. A. *et al.* Non-Fermi-Liquid Behavior of Superconducting SnH<sub>4</sub>. *Advanced Science* (2023) doi:10.1002/advs.202303622.
160. Nakao, H. *et al.* Superconductivity of Pure H<sub>3</sub>S Synthesized from Elemental Sulfur and Hydrogen. *J Physical Soc Japan* **88**, 123701 (2019).
161. Dolui, K. *et al.* Feasible route to high-temperature ambient-pressure hydride superconductivity. (2023) doi:10.48550/arXiv.2310.07562.
162. Eremets, M. I. The current status and future development of high-temperature conventional superconductivity. *Natl Sci Rev* (2024) doi:10.1093/nsr/nwae047.
163. Flores-Livas, J. A. *et al.* A perspective on conventional high-temperature superconductors at high pressure: Methods and materials. *Phys Rep* **856**, 1–78 (2020).
164. Zhang, C. *et al.* Superconductivity in zirconium polyhydrides with T<sub>c</sub> above 70 K. *Sci Bull (Beijing)* **67**, 907–909 (2022).
165. Song, Y. *et al.* Stoichiometric Ternary Superhydride LaBeH<sub>8</sub> as a New Template for High-Temperature Superconductivity at 110 K under 80 GPa. *Phys Rev Lett* **130**, 266001 (2023).
166. Bi, J. *et al.* Giant enhancement of superconducting critical temperature in substitutional alloy (La,Ce)H<sub>9</sub>. *Nat Commun* **13**, 5952 (2022).
167. Li, Z. *et al.* Superconductivity above 70 K observed in lutetium polyhydrides. *Sci China Phys Mech Astron* **66**, 267411 (2023).
168. Wang, Y. *et al.* Synthesis and superconductivity in yttrium superhydrides under high pressure. *Chinese Physics B* **31**, 106201 (2022).
169. Sanna, A. *et al.* Prediction of Ambient Pressure Conventional Superconductivity above 80K in Thermodynamically Stable Hydride Compounds. (2023) doi:10.48550/arXiv.2310.06804.
170. Osmond, I. *et al.* Clean-limit superconductivity in  $\text{I}_3\text{M}^-$  synthesized from sulfur and hydrogen donor ammonia borane. *Phys Rev B* **105**, L220502 (2022).
171. Talantsev, E. F., Crump, W. P., Storey, J. G. & Tallon, J. L. London penetration depth and thermal fluctuations in the sulphur hydride 203 K superconductor. *Ann Phys* **529**, 1–5 (2017).

172. Gao, G. *et al.* Superconducting binary hydrides: Theoretical predictions and experimental progresses. *Materials Today Physics* **21**, 100546 (2021).
173. Song, P. *et al.* (La,Th)H<sub>10</sub>: Potential High- $T_c$  (242 K) Superconductors Stabilized Thermodynamically below 200 GPa. *The Journal of Physical Chemistry C* **128**, 2656–2665 (2024).
174. Gao, K. *et al.* Prediction of high- $T_c$  superconductivity in ternary actinium beryllium hydrides at low pressure. *Phys Rev B* **109**, 014501 (2024).
175. Wang, N. N. *et al.* A low- $T_c$  superconducting modification of Th<sub>4</sub>H<sub>15</sub> synthesized under high pressure. *Supercond Sci Technol* **34**, 034006 (2021).
176. Matsumoto, R. *et al.* Electrical transport measurements for superconducting sulfur hydrides using boron-doped diamond electrodes on beveled diamond anvil. *Supercond Sci Technol* **33**, 124005 (2020).
177. Eremets, M. I., Trojan, I. A., Medvedev, S. A., Tse, J. S. & Yao, Y. Superconductivity in Hydrogen Dominant Materials: Silane. *Science (1979)* **319**, 1506–1509 (2008).
178. Wang, T. *et al.* Absence of conventional room-temperature superconductivity at high pressure in carbon-doped H<sub>3</sub>S. *Phys Rev B* **104**, 064510 (2021).
179. Sun, Y., Zhong, X., Liu, H. & Ma, Y. Clathrate metal superhydrides at high-pressure conditions: enroute to room-temperature superconductivity. *Natl Sci Rev* (2023) doi:10.1093/nsr/nwad270.
180. Bhattacharyya, P. *et al.* Imaging the Meissner effect in hydride superconductors using quantum sensors. *Nature* (2024) doi:10.1038/s41586-024-07026-7.
181. Ho, K. O. & Yang, S. Quantum sensor settles debate about superconductivity in hydrides. *Nature* (2024) doi:10.1038/d41586-024-00423-y.
182. Xiong, C. *et al.* Effect of physical and chemical pressure on the superconductivity of cage-type compound Lu<sub>5</sub>Rh<sub>6</sub>Sn<sub>18</sub>. *Phys Rev B* **109**, 075202 (2024).
183. Sun, H. *et al.* Signatures of superconductivity near 80 K in a nickelate under high pressure. *Nature* **621**, 493–498 (2023).
184. He, X. *et al.* Superconductivity above 30 K achieved in dense scandium. (2023) doi:https://doi.org/10.48550/arXiv.2303.01062.
185. Ying, J. *et al.* Record High 36 K Transition Temperature to the Superconducting State of Elemental Scandium at a Pressure of 260 GPa. *Phys Rev Lett* **130**, 256002 (2023).
186. Zhang, C. *et al.* Record high  $T_c$  element superconductivity achieved in titanium. *Nat Commun* **13**, 5411 (2022).
187. Liu, X. *et al.*  $T_c$  up to 23.6 K and robust superconductivity in the transition metal  $\delta$ -Ti phase at megabar pressure. *Phys Rev B* **105**, 224511 (2022).
188. Guo, J. *et al.* Electron-hole balance and the anomalous pressure-dependent superconductivity in black phosphorus. *Phys Rev B* **96**, 224513 (2017).
189. Li, C. *et al.* Pressure-Tuning Superconductivity in Noncentrosymmetric Topological Materials ZrRuAs. *Materials* **15**, 7694 (2022).
190. Zhou, Y. *et al.* Quantum phase transition from superconducting to insulating-like state in a pressurized cuprate superconductor. *Nat Phys* **18**, 406–410 (2022).
191. Pei, C. *et al.* Pressure-induced superconductivity in topological heterostructure (PbSe)<sub>5</sub>(Bi<sub>2</sub>Se<sub>3</sub>)<sub>6</sub>. *Sci China Mater* (2023) doi:10.1007/s40843-022-2422-3.
192. Jin, M. *et al.* Pressure Tuned 2D Superconductivity in Black Phosphorus. (2023).
193. Li, X. *et al.* Pressure-induced phase transitions and superconductivity in a black phosphorus single crystal. *Proceedings of the National Academy of Sciences* **115**, 9935–9940 (2018).
194. Guo, J. *et al.* Crossover from two-dimensional to three-dimensional superconducting states in bismuth-based cuprate superconductor. *Nat Phys* **16**, 295–300 (2020).
195. Guo, J. *et al.* Robust zero resistance in a superconducting high-entropy alloy at pressures up to 190 GPa. *Proceedings of the National Academy of Sciences* **114**, 13144–13147 (2017).
196. Pei, C. *et al.* Distinct superconducting behaviors of pressurized WB<sub>2</sub> and ReB<sub>2</sub> with different local B layers. *Sci China Phys Mech Astron* **65**, 287412 (2022).
197. Pei, C. *et al.* Pressure-induced superconductivity at 32 K in MoB<sub>2</sub>. *Natl Sci Rev* **10**, (2023).
198. Wu, Y. Y. *et al.* Pressure-induced superconductivity in the van der Waals semiconductor violet phosphorus. (2023) doi:https://doi.org/10.48550/arXiv.2307.02989.
199. Shimizu, K. Superconducting elements under high pressure. *Physica C: Superconductivity and its Applications* **552**, 30–33 (2018).
200. Eremets, M. I., Shimizu, K., Kobayashi, T. C. & Amaya, K. Metallic CsI at Pressures of up to 220 Gigapascals. *Science (1979)* **281**, 1333–1335 (1998).

201. Shimizu, K., Suhara, K., Ikumo, M., Eremets, M. I. & Amaya, K. Superconductivity in oxygen. *Nature* **393**, 767–769 (1998).
202. Talantsev, E. Classifying Charge Carrier Interaction in Highly Compressed Elements and Silane. *Materials* **14**, 4322 (2021).
203. Zhang, H. *et al.* Superconductivity above 12 K with possible multiband features in CsCl-type PbS. *Phys Rev B* **107**, 174502 (2023).
204. Grinenko, V. *et al.* Unsplit superconducting and time reversal symmetry breaking transitions in Sr<sub>2</sub>RuO<sub>4</sub> under hydrostatic pressure and disorder. *Nat Commun* **12**, 3920 (2021).
205. Pei, C. *et al.* Pressure-induced reemergence of superconductivity in BaIr<sub>2</sub>Ge<sub>7</sub> and Ba<sub>3</sub>Ir<sub>4</sub>Ge<sub>16</sub> with cage structures. *Matter and Radiation at Extremes* **7**, (2022).
206. Bhattacharyya, A. *et al.* Exploring superconductivity in Ba<sub>3</sub>Ir<sub>4</sub>Ge<sub>16</sub>: Experimental and theoretical insights. *J Alloys Compd* **978**, 173374 (2024).
207. Cao, Z.-Y. *et al.* Spectroscopic evidence for the superconductivity of elemental metal Y under pressure. *NPG Asia Mater* **15**, 5 (2023).
208. Huyan, S. *et al.* Suppression of metal-to-insulator transition and stabilization of superconductivity by pressure in Re<sub>3</sub>Ge<sub>7</sub>. (2024).
209. Rana, K. *et al.* Impact of nematicity on the relationship between antiferromagnetic fluctuations and superconductivity in FeSe<sub>0.91</sub>S<sub>0.09</sub> under pressure. *Phys Rev B* **101**, 180503 (2020).
210. Sadakoy, A. V. *et al.* Multiband Superconductivity in KCa<sub>2</sub>Fe<sub>4</sub>As<sub>4</sub>F<sub>2</sub>. *JETP Lett* (2024) doi:10.1134/S0021364023603676.
211. Rivasto, E., Aye, M. M., Huhtinen, H. & Paturi, P. Enhanced critical current density in optimized high-temperature superconducting bilayer thin films. *Journal of Physics: Condensed Matter* **36**, 135702 (2024).
212. Jung, S. *et al.* A Quenched Disorder in the Quantum-Critical Superconductor CeCoIn<sub>5</sub>. *Advanced Science* **11**, (2024).
213. Hamill, A. *et al.* Two-fold symmetric superconductivity in few-layer NbSe<sub>2</sub>. *Nat Phys* **17**, 949–954 (2021).
214. Zhang, H. *et al.* Tailored Ising superconductivity in intercalated bulk NbSe<sub>2</sub>. *Nat Phys* **18**, 1425–1430 (2022).
215. Park, S. *et al.* Superconductivity emerging from a stripe charge order in IrTe<sub>2</sub> nanoflakes. *Nat Commun* **12**, 3157 (2021).
216. Gumeniuk, R., Levytskyi, V., Kundys, B. & Leithe-Jasper, A. Yb<sub>3</sub>Rh<sub>4</sub>Sn<sub>13</sub>: Two-gap superconductor with a complex Fermi surface. *Phys Rev B* **108**, 214515 (2023).
217. Leung, C. K. W., Zhang, X., von Rohr, F., Lortz, R. & Jäck, B. Evidence for isotropic s-wave superconductivity in high-entropy alloys. *Sci Rep* **12**, 1–7 (2022).
218. Shang, T. *et al.* Fully gapped superconductivity with preserved time-reversal symmetry in NiBi<sub>3</sub> single crystals. *Phys Rev B* **107**, 174513 (2023).
219. Zhang, W. *et al.* Nodeless Superconductivity in Kagome Metal CsV<sub>3</sub>Sb<sub>5</sub> with and without Time Reversal Symmetry Breaking. *Nano Lett* **23**, 872–879 (2023).
220. Li, D. *et al.* Superconductivity in an infinite-layer nickelate. *Nature* **572**, 624–627 (2019).
221. Osada, M. *et al.* A Superconducting Praseodymium Nickelate with Infinite Layer Structure. *Nano Lett* **20**, 5735–5740 (2020).
222. Lee, K. *et al.* Linear-in-temperature resistivity for optimally superconducting (Nd,Sr)NiO<sub>2</sub>. *Nature* **619**, 288–292 (2023).
223. Wang, B. Y. *et al.* Effects of rare-earth magnetism on the superconducting upper critical field in infinite-layer nickelates. *Sci Adv* **9**, (2023).
224. Kang, M. *et al.* Charge order landscape and competition with superconductivity in kagome metals. *Nat Mater* (2022) doi:10.1038/s41563-022-01375-2.
225. Oey, Y. M., Kaboudvand, F., Ortiz, B. R., Seshadri, R. & Wilson, S. D. Tuning charge density wave order and superconductivity in the kagome metals KV<sub>3</sub>Sb<sub>5-x</sub>Sn<sub>x</sub> and RbV<sub>3</sub>Sb<sub>5-x</sub>Sn<sub>x</sub>. *Phys Rev Mater* **6**, 074802 (2022).
226. Wang, Y., Wu, H., McCandless, G. T., Chan, J. Y. & Ali, M. N. Quantum states and intertwining phases in kagome materials. *Nature Reviews Physics* **5**, 635–658 (2023).
227. Yip, K. Y. *et al.* Shubnikov–de Haas oscillations of biaxial-strain-tuned superconductors in pulsed magnetic field up to 60 T. *APL Mater* **12**, (2024).
228. Wang, Y. *et al.* Nontrivial Fermi surface topology and large anomalous Hall effect in the kagome superconductor RbV<sub>3</sub>Sb<sub>5</sub>. *Phys Rev B* **108**, 035117 (2023).

229. Wang, L. *et al.* Anomalous Hall effect and two-dimensional Fermi surfaces in the charge-density-wave state of kagome metal  $\text{RbV}_3\text{Sb}_5$ . *Journal of Physics: Materials* **6**, 02LT01 (2023).
230. Koblishchka, M. R. & Koblishchka-Veneva, A. Review of Moiré superconductivity and application of the Roeser-Huber formula. *Superconductivity* **9**, 100073 (2024).
231. Li, Z. *et al.* Charge fluctuations, phonons, and superconductivity in multilayer graphene. *Phys Rev B* **108**, 045404 (2023).
232. Kamihara, Y., Watanabe, T., Hirano, M. & Hosono, H. Iron-Based Layered Superconductor  $\text{La}[\text{O}_{1-x}\text{F}_x]\text{FeAs}$  ( $x = 0.05\text{--}0.12$ ) with  $T_c = 26$  K. *J Am Chem Soc* **130**, 3296–3297 (2008).
233. Takahashi, H. *et al.* Superconductivity at 43 K in an iron-based layered compound  $\text{LaO}_{1-x}\text{F}_x\text{FeAs}$ . *Nature* **453**, 376–378 (2008).
234. Kamihara, Y. *et al.* Iron-Based Layered Superconductor:  $\text{LaOFeP}$ . *J Am Chem Soc* **128**, 10012–10013 (2006).
235. Iida, K., Hänisch, J., Hata, S. & Yamamoto, A. Recent progress on epitaxial growth of Fe-based superconducting thin films. *Supercond Sci Technol* **36**, 063001 (2023).
236. Cayado, P., Hänisch, J., Iida, K. & Senatore, C. Focus on recent advances in superconducting films. *Supercond Sci Technol* **36**, 090401 (2023).
237. Jung, S.-G. *et al.* Manipulating superconducting phases via current-driven magnetic states in rare-earth-doped  $\text{CaFe}_2\text{As}_2$ . *NPG Asia Mater* **10**, 156–162 (2018).
238. Jung, S.-G. *et al.* High critical current density and high-tolerance superconductivity in high-entropy alloy thin films. *Nat Commun* **13**, 3373 (2022).
239. Seo, S. *et al.* Artificially engineered nanostrain in  $\text{FeSe}_x\text{Te}_{1-x}$  superconductor thin films for supercurrent enhancement. *NPG Asia Mater* **12**, 7 (2020).
240. Jung, S.-G. *et al.* Field-induced quantum breakdown of superconductivity in magnesium diboride. *NPG Asia Mater* **13**, 55 (2021).
241. Kawachi, S. *et al.* Distinctive doping dependence of upper critical field in iron-based superconductor  $\text{LaFeAsO}_{1-x}\text{H}_x$ . *Phys Rev B* **108**, L100503 (2023).
242. Kim, H. *et al.* Nodal superconductivity in miassite  $\text{Rh}_1\text{7S}_{15}$ . *Commun Mater* **5**, 17 (2024).
243. Haberkorn, N., Ribeiro, R. A., Xiang, L., Bud'ko, S. L. & Canfield, P. C. Superconducting properties and vortex pinning in intermetallic  $\text{BaBi}_3$  single crystals: A magnetization study. *Physica C: Superconductivity and its Applications* **615**, 1354387 (2023).
244. Kim, Y. H. *et al.* Two-dimensional multiband superconductivity of the optimally and uniformly Li-intercalated  $\text{FeSe}$  nanoflakes. *Current Applied Physics* **46**, 27–33 (2023).
245. Xu, M. *et al.* Superconductivity and magnetic and transport properties of single-crystalline  $\text{CaK}(\text{Fe}_{1-x}\text{Cr}_x)_4\text{As}_4$ . *Phys Rev B* **107**, 134511 (2023).
246. Bud'ko, S. L., Xu, M. & Canfield, P. C. Trapped flux in pure and Mn-substituted  $\text{CaKFe}_4\text{As}_4$  and  $\text{MgB}_2$  superconducting single crystals. *Supercond Sci Technol* **36**, 115001 (2023).
247. Canfield, P. C., Bud'ko, S. L. & Finnemore, D. K. An overview of the basic physical properties of  $\text{MgB}_2$ . *Physica C Supercond* **385**, 1–7 (2003).
248. Bergmann, G. Amorphous metals and their superconductivity. *Phys Rep* **27**, 159–185 (1976).
249. Dutta, S. *et al.* Superconductivity in amorphous  $\text{Re Zr}$  ( $x \approx 6$ ) thin films. *J Alloys Compd* **877**, 160258 (2021).
250. Zhang, K. *et al.* Superconducting Phase Induced by a Local Structure Transition in Amorphous  $\text{Sb}_2\text{Se}_3$  under High Pressure. *Phys Rev Lett* **127**, 127002 (2021).
251. Terashima, T. *et al.* Anomalous upper critical field in the quasicrystal superconductor  $\text{Ta}_{1.6}\text{Te}$ . (2024).
252. Gebresenbut, G. H. *et al.* Superconducting  $\text{YAu}_3\text{Si}$  and Antiferromagnetic  $\text{GdAu}_3\text{Si}$  with an Interpenetrating Framework Structure Built from 16-Atom Polyhedra. *Inorg Chem* **61**, 4322–4334 (2022).
253. Shiino, T. *et al.* Superconductivity at 1 K in Y-Au-Si quasicrystal approximants. *Phys Rev B* **103**, 054510 (2021).
254. Tokumoto, Y. *et al.* Superconductivity in a van der Waals layered quasicrystal. *Nat Commun* **15**, 1529 (2024).
255. Malykhin, S. V. *et al.* Structure and electrical conductivity of Ti-Zr-Ni films of quasicrystalline and related crystalline phases. *J Alloys Compd* **965**, 171386 (2023).
256. Kamiya, K. *et al.* Discovery of superconductivity in quasicrystal. *Nat Commun* **9**, 154 (2018).

## Supplementary Materials

### La<sub>4</sub>H<sub>23</sub> superconductor: Nanograined structure, low nanocrystalline strain, strong electron-phonon interaction, and moderate level of nonadiabaticity

#### I. XRD scans and data fit to multiple Lorentz function for data reported by Cross *et al.*<sup>44</sup>.

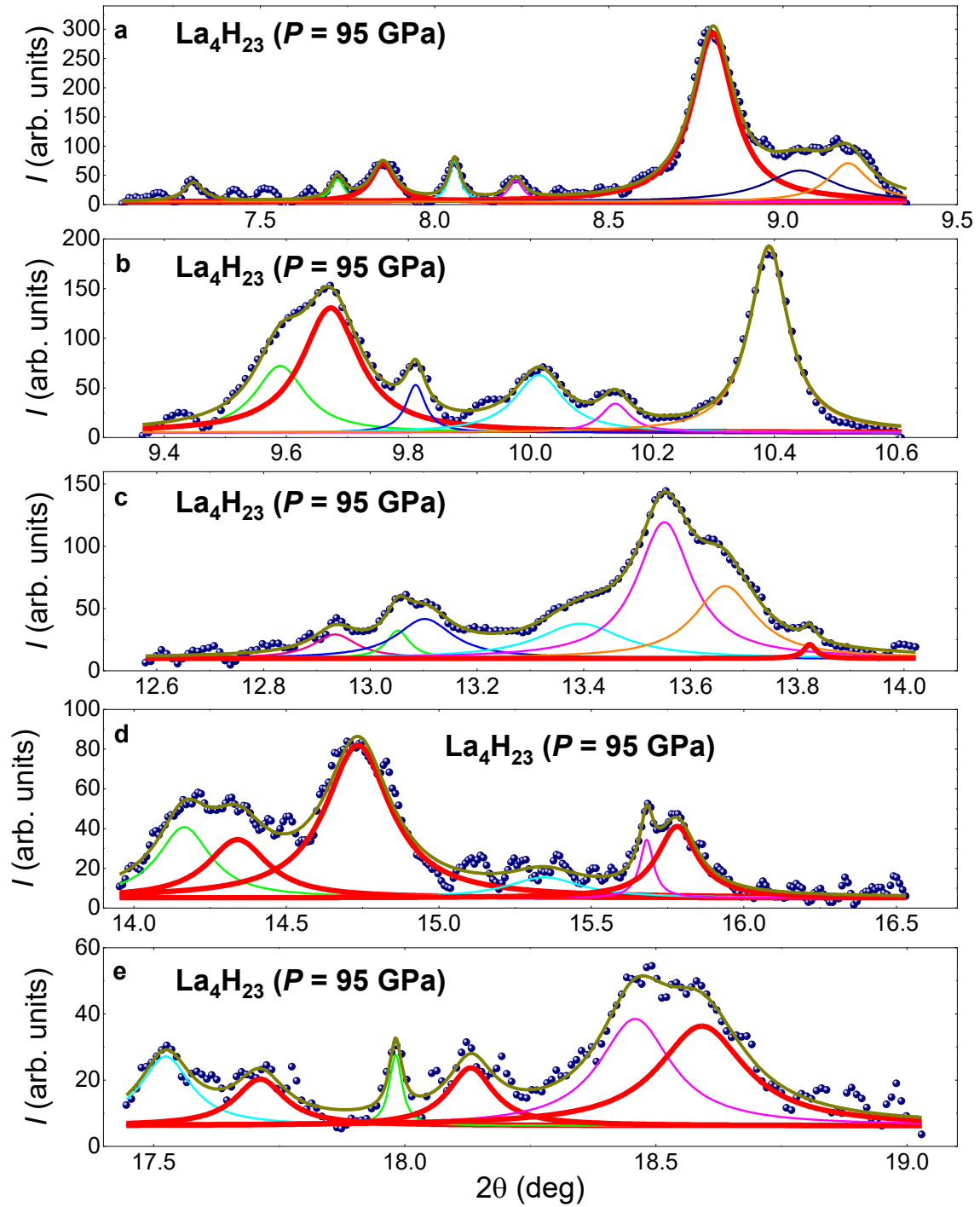


**Figure S1.** XRD scans and data fits to multiple Lorentz peaks function for raw data reported by Cross *et al.*<sup>44</sup> for La<sub>4</sub>H<sub>23</sub> compressed at  $P = 95$  GPa.



II. XRD scans and data fit to multiple Lorentz function for data reported by Guo *et al* [42].

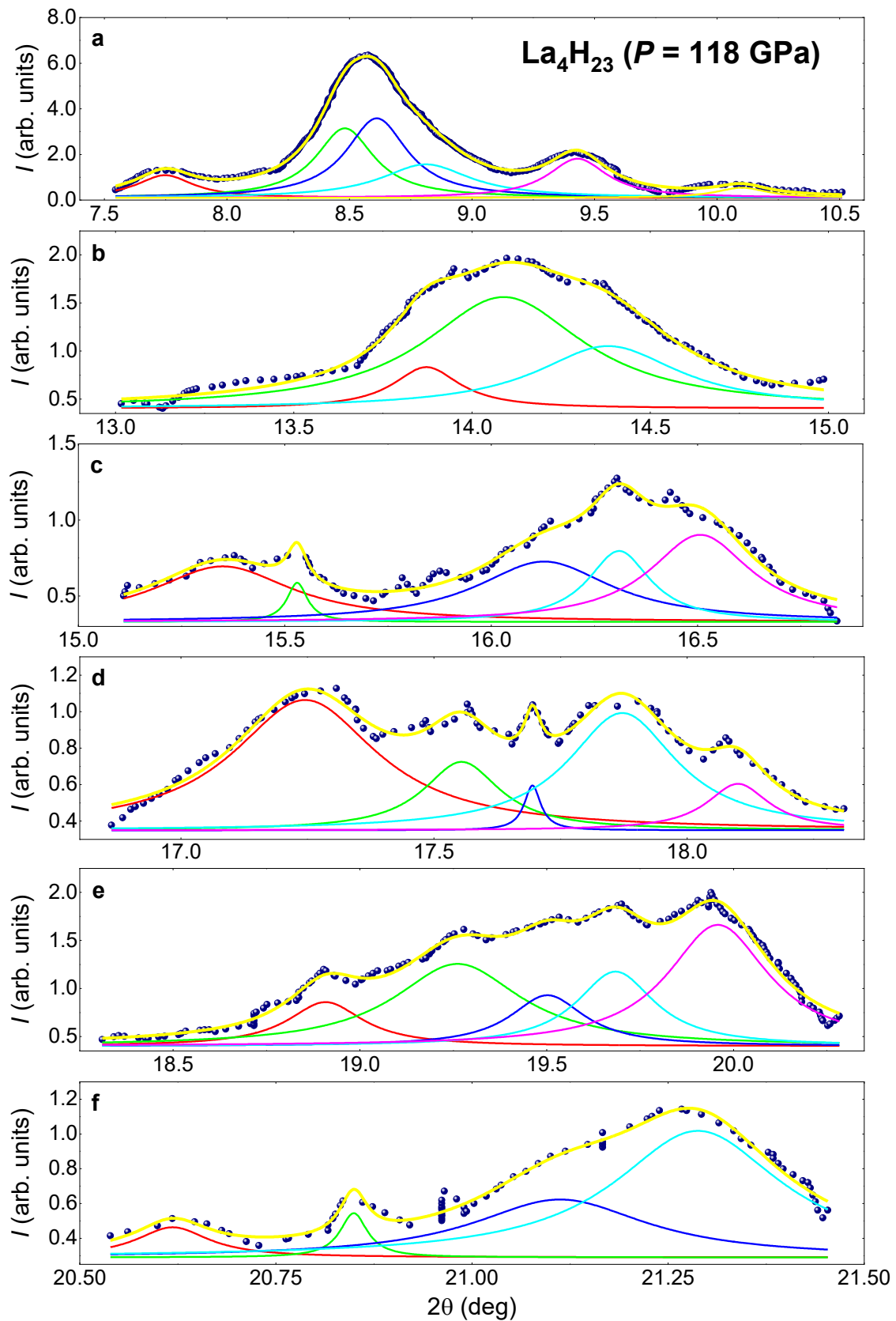


**Figure S2.** XRD scans and data fits to multiple Lorentz peaks function for raw data reported by Guo *et al* [42] for  $\text{La}_4\text{H}_{23}$  compressed at  $P = 118$  GPa.

### III. Function used to fit $R(T)$ data for sample reported by Sakata *et al*<sup>41</sup>

In Figures 4 we showed the  $R(T)$  curve to the fitting function:

$$R(T) = \frac{1}{\frac{1}{R_{sat}} + \frac{1}{R_0 + \theta(T - T_C) \times \left( \frac{R_n}{I_0^2 \left( C \times \left| 1 - \frac{T}{T_C} \right|^{1.5} \right)} \right) + \theta(T - T_C) \times \left( R_n - A \times \left( \left( \frac{T_C}{\Theta_D} \right)^5 \times \int_0^{\frac{\Theta_D}{T_C}} \frac{x^5}{(e^x - 1)(1 - e^{-x})} dx - \left( \frac{T}{\Theta_D} \right)^5 \times \int_0^{\frac{\Theta_D}{T}} \frac{x^5}{(e^x - 1)(1 - e^{-x})} dx \right)}}} \quad (S1)$$

where  $R_{sat}$ ,  $R_0$ ,  $C$ ,  $T_C$ ,  $R_n$ ,  $A$ ,  $\Theta_D$  are free-fitting parameters,  $\theta(x)$  is the Heaviside step function, and  $I_0(x)$  is the zero-order modified Bessel function of the first kind.